Assessment of Sentinel-3 Altimeter Performance over Antarctica using High Resolution Digital Elevation Models

Abstract

Since 2016, the Sentinel-3 satellites have provided a continuous record of ice sheet elevation and elevation change. Given the unique, operational nature of the mission, and the planned launch of two additional satellites before the end of this decade, it is important to determine the performance of the altimeter across a range of ice sheet topographic surfaces. Whilst previous studies have assessed elevation accuracy, more detailed investigations of the underlying instrument and processor performance are lacking. This study therefore examines the performance of the Sentinel-3 Synthetic Aperture Radar (SAR) altimeter over the Antarctic Ice Sheet (AIS), utilising new detailed topographic information from the Reference Elevation Model of Antarctica (REMA). Applying Singular Value Decomposition to REMA, we firstly develop new self-consistent Antarctic surface slope and roughness datasets. We then use these datasets to assess altimeter performance across different topographic regimes, targeting a number of key steps in the altimeter processing chain. We also evaluate the impact of topography upon waveform decorrelation. ~~We~~For the new Sentinel-3 Thematic Product, we find that, for ~~90~~94.1% of acquisitions, the point of closest approach to the satellite is successfully captured within the ~~Level-1b~~ range window~~. However~~ - an improvement of ~5% compared to the previous non-thematic (BC-004) product. For both products, performance ~~degrades~~declines with increasing topographic complexity, ~~and this~~which also ~~affects~~limits the ~~capacity~~ability to record all backscattered energy ~~from~~ within the beam footprint. We ~~find~~estimate that ~~24~~57.4% of the ice sheet exhibits greater topographic variance within the footprint than can be captured by the range window, and that the current window placement captures a median of ~~90~~89.2% of the total possible topography that could be recorded. These findings provide a better understanding of the performance of the Sentinel-3 altimeters over ice sheets, and can guide the design and optimisation of future satellite missions such as the Copernicus Polar Ice and Snow Topography Altimeter (CRISTAL~~).~~) and the Sentinel-3 Next Generation Topography mission.

From 1992 to 2020, the Antarctic Ice Sheet (AIS) lost a total of 2671 $\pm$ 530 billion tonnes of ice (Otosaka et al., 2023), with current rates of ice loss now ~6 times greater than those measured in 1979 (Rignot et al., 2019). Recent studies suggest that this accelerating loss of ice, which has occurred mostly across sectors of West Antarctica and the Antarctic Peninsula, increased global sea levels by 7.4 $\pm$ 1.5 mm from 1992 to 2020 (Otosaka et al., 2023). As Earth's climate continues to warm, current projections suggest that the sea level contribution from the AIS will reach multiple decimetres by 2100, with high-end projections exceeding 1 m (Frederikse et al., 2020). This large range in projections, whilst partly due to a variety of forcing pathways, is also linked to uncertainty in the physical processes governing the ice sheet's response to climate change. Within this context, it is imperative to establish and maintain long-term monitoring programmes to better understand the physical processes that control ongoing ice sheet imbalance (Davis et al., 2005; Price et al., 2011; Shepherd et al., 2004). Whilst a range of techniques exist for remote observation of the cryosphere, our understanding of how ice sheets are changing is largely informed by satellite observations, with the longest continuous record coming from the technique of

satellite radar altimetry. The principal use of altimetry over ice sheets is to derive estimates of ice sheet elevation and elevation change (Shepherd et al., 2019; ~~D. J.~~ Wingham et al., 1998), which, ultimately, can be used to determine ice sheet mass imbalance. Radar altimeters have also been used to investigate a range of other glaciological processes, including grounding line location and migration (Dawson & Bamber, 2017; ~~Rignot~~Hogg et al., ~~2011~~2018; Konrad et al., 2018), subglacial hydrology (~~Siegert~~Gourmelen et al., ~~2016~~2017; McMillan et al., 2013; Siegfried & Fricker, 2018; Wingham, Siegert, et al., 2006), ice shelf processes (Chuter & Bamber, 2015; Griggs & Bamber, 2011), and surface mass balance (~~Pritchard et al., 2010; Simonsen~~Slater et al., 2021).

The initiation of continuous ice sheet monitoring by altimetry began with the launch of the ERS-1 mission in the early 1990s, albeit ERS-1 was designed primarily to measure the ocean geoid. Continuity during the following two decades was provided by the ERS-2 and Envisat satellite missions, before the launch of CryoSat-2 (CS2) in 2010 introduced technical innovations specifically tailored for ice surfaces. Subsequently, Sentinel-3 (S3), which to date comprises two satellites launched in 2016 and 2018, ushered in an era of operational monitoring and global Synthetic Aperture Radar (SAR) coverage, thus representing another significant milestone in the historical progression of satellite altimetry (Abdalla et al., 2021).

The measurements made by radar altimeters over the past 30 years have provided important new insight into the changing nature of Earth's ice sheets. However, like all geodetic techniques, the fidelity of measurements varies, as a consequence of both the instrument design and the complexity of the illuminated ice surface. In the case of radar altimeters, measurement quality typically degrades with increasing topographic complexity, due to the difficulty of keeping track of the ice surface, the failure of assumptions ~~made within the~~used in Level-2 processing under such conditions, and the limitations ~~imposed by~~of the ~~instrument~~instrument's spatial resolution. Whilst a number of previous studies (~~Brenner~~Aublanc et al., ~~2007~~2025; Clerc, Donlon, Borde, Lamquin, Hunt, Smith, McMillan, Mittaz, Woolliams, Hammond, Banks, et al., 2020; McMillan et al., 2019, 2021; Quartly~~, Nencioli, Raynal, Bonnefond, Nilo Garcia, Garcia-Mondéjar, Flores de la Cruz, Crétaux, Taburet, Frery, Cancet,~~ et al., 2020) have quantified the overall accuracy of elevation measurements derived from the Sentinel-3 altimeter, less attention has been given to investigating the underlying performance of the instrument and, ultimately, how characteristics relating to the instrument and algorithm design have affected the ability of the altimeter to make reliable elevation retrievals. With the recent availability of high resolution Digital Elevation Models, such as the Reference Elevation Model of Antarctica (REMA; ~~(~~I. M. Howat et al~~.,~~. (2019)), comes the opportunity to evaluate a number of these design choices, and therefore to advance our understanding of altimeter performance. This, in turn, can benefit the design and operation of future altimeter missions. In this study, we therefore use REMA to undertake a detailed evaluation of Sentinel-3 elevation retrievals across the Antarctic Ice Sheet, in order to better understand the impact of topographic characteristics on altimeter performance.

Principles of Radar Altimetry

In this section we briefly review the principles governing the acquisition and processing of radar altimeter echoes over ice sheet surfaces, which provides the context for the analysis presented in this study. Radar altimeters work by transmitting a short radio-wave pulse towards Earth's surface and recording the returned echo in the form of a discretised waveform. Each recorded waveform, comprising the sum of incident surface reflections from within the altimeter footprint ordered by arrival time (Brown, 1977), encodes information pertaining to the surface illuminated by the satellite, such as topography, electromagnetic scattering characteristics, and in the case of returns over ocean, wind speed and significant wave height (Quartly~~, Nencioli, Raynal, Bonnefond, Nilo Garcia, Garcia-Mondéjar, Flores de la Cruz, Crétaux, Taburet, Frery, & others, 2020).~~ et al., 2020). Over uniform surfaces, altimeter waveforms take a distinctive shape, with a clear peak in power, corresponding to the first return from the surface at the point~~-~~ of~~-~~ closest~~-~~approach (POCA) to the satellite, followed by a gradual decay in the received power - due to the combined influence of the antenna gain pattern and the orientation of the surface relative to the incident radar wave.

For echoes acquired over ice sheet surfaces, however, and in particular in regions close to the ice margins, waveform shape can be more complex, due to numerous discrete~~, equidistant~~ regions of backscatter within the illuminated beam-limited footprint. Nonetheless, from each recorded echo, an estimate of surface elevation can be derived by measuring the range between the satellite and a fixed point on the leading edge of the waveform, which is assumed (in the case of ~~non-interfrometric~~conventional altimetry) to correspond to the POCA return. This range measurement can then be converted to an estimate of the surface elevation at the POCA, given knowledge of the satellite altitude. ~~In addition,~~Additionally, several other useful descriptive parameters can also be derived from the waveform, including estimates of (1) the ice sheet's backscatter coefficient (sigma-0~~)~~), which can be used to characterise ice sheet properties such as snow depth, grain size, and density (Blarel et al., 2015; Mertikas et al., 2020); (2) the leading edge width, which contains information related to surface roughness and radar wave penetration into the near-surface snow layer; and (3) the trailing edge slope, which is sensitive to both footprint scale topography and subsurface backscattering (Legresy et al., 2005; Rémy & Parouty, 2009).

In practice, the retrieval of ice sheet elevation measurements involves a number of onboard and on-ground processing steps, relating to the acquisition and subsequent processing of the altimeter echo. These include (1) surface tracking, (2) retracking, (3) determination of POCA, and (4) geophysical and instrumental corrections, and are described in turn below.

Surface Tracking

In order to capture the backscattered radar pulse that forms each waveform, the altimeter records the incoming energy for a discrete amount of time, corresponding to when it

expects the reflection to be received from the surface. Radar altimeters can have a recording window as ~~low~~short as several microseconds, and when this fails to coincide with the surface return then the instrument temporarily loses track of Earth's surface. Therefore, in order to capture returns effectively, an altimeter requires an estimate of the predicted range to the approaching surface. To provide such information, two methods are utilised: "closed-loop" and "open-loop" tracking. Closed-loop tracking predicts the next range based on the history of the last few seconds. Whilst this works well when the range has linear variation, such as over the ocean or the low slope interiors of the ice sheets, its performance degrades over more highly variable terrain, because the range history is a less reliable predictor of the future range evolution ~~(Quartly, Nencioli, Raynal, Bonnefond, Nilo Garcia, Garcia-Mondéjar, Flores de la Cruz, Crétaux, Taburet, Frery, Cancet, et al., 2020).~~ In contrast, open-loop tracking uses information from an a priori Digital Elevation Model (DEM) to provide the satellite with an estimate of the expected range to the ice surface~~.~~ (Donlon, Berruti, Buongiorno, et al., 2012). This method~~, first applied onboard the Jason-2 mission,~~ has the potential to more precisely track the complex topography ~~that is~~ found across many parts of the ice sheet margin. ~~However, with~~Open loop tracking was first applied onboard the Jason-2 mission, which over land utilised the ~~exception of~~ESA ACE-1 DEM at 1 km resolution (Birkett & Beckley, 2010). It has subsequently been used by Sentinel-~~3A's~~3 during commissioning ~~phase,~~ and ~~isolated~~ ad hoc ~~acquisitions, it remains largely untested to date over~~ tasking over land ice ~~sheet~~ surfaces ~~(Donlon, Berruti, Buongiorno, et al., 2012; Quartly, Nencioli, Raynal, Bonnefond, Nilo Garcia, Garcia-Mondéjar, Flores de la Cruz, Crétaux, Taburet, Frery, Cancet, et al., 2020).~~, and is planned to be implemented operationally onboard CRISTAL.

Retracking

During Level-2 (L2) processing, the position of the waveform leading edge relative to a specific onboard tracking gate is estimated. This process is known as "retracking~~".~~", and can involve adjusting the tracker range by several meters (Martin et al., 1983; Ridley & Partington, 1988). In general, retracking algorithms can be categorised as "physical" or "empirical". Physical retrackers fit an analytical model to the received waveform in order to represent the underlying physics of the radar wave's interaction with the scattering surface, whereas empirical retrackers solely consider the geometry of the recorded waveform (Passaro et al., 2022; Villadsen et al., 2016). In practice, physical retrackers are rarely used over ice sheets, because ~~they are too sensitive~~of their inability to fit irregular waveform shapes caused by complex terrain, and their sensitivity to changes in the scattering properties of the surface (~~Quartly, Nencioli, Raynal, Bonnefond, Nilo Garcia, Garcia-Mondéjar, Flores de la Cruz, Crétaux, Taburet, Frery, Cancet,~~Landy et al., 2019; Martin et al., 1983; Quartly et al., 2019, 2020; Slater et al., 2019). Conversely, empirical retrackers do not assume waveform shape, and as such, are far more robust to cases where the echo deviates from its theoretical shape. Examples of physical and semi-analytical retrackers include Ice-2 (~~Ehlers~~Legresy et al., ~~2023);~~2005), which was applied to low resolution mode ENVISAT data, ~~and~~ SAMOSA (Ray et al., 2015), which has been applied to delay-doppler Cryosat-2 and Sentinel-3 data~~.~~, and the UCL ice sheet retracker

(Wingham, Francis, et al., 2006), which is deployed in the Sentinel-3 land ice ground segment. Examples of empirical retrackers include ICE-1, which applies a threshold based upon the OCOG (Offset Centre of Gravity) amplitude (and, 1994; D. Wingham et al., 1986), and has been used widely since its implementation within the ground segment of ERS-1; the threshold retracker developed by Davis (1997); TFMRA (Threshold First Maximum Re-tracker Algorithm) (Helm et al., 2014~~) and a threshold OCOG (Offset Centre of Gravity) (D. Wingham~~); and MultiPeak Ice (MPI), a recent approach designed to handle complex, multi-peaked waveforms (Huang et al., ~~1986), the latter of which is deployed in~~2024). Within the Sentinel-3 land ice ground segment processing, both the UCL retracker and a threshold OCOG retracker are implemented.

Determination of the Point of Closest Approach

As the measured range to the POCA is 1-dimensional, it is insufficient to determine the location of POCA in 3-dimensional space; rather it constrains POCA to lie upon an iso-range surface, a constant distance from the satellite. Solving for this ambiguity – to determine the location of POCA – is ~~known~~ a process commonly referred to as slope~~-~~ correction. Specifically, the aim is to identify the origin on the surface corresponding to the measured elevation, based upon the assumption that the point closest to the satellite corresponds to the backscattered energy from the leading edge of the waveform. Over rugged terrain, the magnitude of this slope correction can reach tens of meters vertically, and several kilometers across-track. As such, uncertainties in applying ~~the~~this correction ~~represent a significant~~are commonly the largest source of uncertainty in non-interferometrically derived elevation measurements (Brenner et al., 2007; Li et al., 2022).

Historically, to identify the POCA location, “slope-based” methods were used~~-~~ (and, 1994; Brenner et al., 1983; Cooper, 1989; Remy et al., 1989). These assumed a constant slope within the beam-limited altimeter footprint, which was commonly derived using a priori slope data at nadir (Levinsen et al., ~~2016~~2016a; Remy et al., 1989). By assuming an orthogonal reflection from the surface, the approximate location of the POCA can then be determined using trigonometry (Brenner et al., 1983; Roemer et al., 2007). Whilst the assumption of constant slope is reasonable over simpler, homogeneous terrain, the slope method neglects the finer-scale topography within the beam~~-~~-limited footprint, which may lead to inaccuracies over ~~more~~even moderately undulating areas of the ice sheet (Levinsen et al., ~~2016~~2016a). To address this, “point-based” methods were developed which locate the POCA by using a DEM to search for points with minimum range within the beam-limited satellite footprint~~-~~ (Levinsen et al., ~~2016~~2016a; Li et al., 2022; Roemer et al., 2007). Such an approach was first introduced by Roemer et al. (2007~~), who found that it outperformed slope-based methods over Lake Vostok within the East Antarctic interior. More specifically, the method~~) using a DEM derived from ERS-1 measurements. Specifically, this approach moves a fixed window the approximate size of the satellite’s pulse-limited footprint through DEM data within the beam-limited footprint (Roemer et al., 2007). The POCA location is then identified as the centroid of the window that minimises the mean range between the satellite and the DEM points within that window, with interpolation between DEM nodes used to further improve accuracy and precision. In their initial study,

Roemer et al. (2007) found that this new approach outperformed slope-based methods over Lake Vostok within the East Antarctic interior, reducing the error standard deviation from 1.1 m to ~0.5 m when compared to ICESat-1 measurements. This was subsequently confirmed over Greenland, both for Envisat (Levinsen et al., 2016b) and CryoSat-2 (Li et al., 2022) Low Resolution Mode data. In both cases the dispersion of the elevation differences relative to either airborne or satellite laser altimetry was 2-6 times greater for a slope-based approach in comparison to a point-based approach.

More recently, LEPTA (Leading Edge Point Based), a formulation of a point-based method was proposed by Li et al. (2022), which utilised the ranges spanned by the waveform leading edge to identify the DEM points corresponding to the POCA. The POCA, and consequently the slope correction, ~~is~~was then derived from the mean of ~~these~~the points~~, with this~~ intersecting the leading edge. This approach has also ~~generalisable~~been generalised to allow retrieval of multiple elevations from a single multi-peaked waveform, which was demonstrated for Sentinel-3 SAR acquisitions (Huang et al., 2024). ~~These methods, referred to as~~When benchmarked against ICESat-2, LEPTA ~~and MPI respectively, were found to outperform other methods in the derivation~~achieved a median height difference of ~~ice sheet~~< 0.01 m and a median absolute deviation of 0.09 m. However, it remains sensitive to DEM biases and temporal elevation~~. More recently still, the~~ changes due to its reliance on a static DEM (Huang et al., 2024; Li et al., 2022). Finally, AMPLI ~~model was introduced by~~ (Altimeter data Modelling and Processing for Land Ice) (Aublanc~~et al. (2024), which further enhances the accuracy of POCA location determination by employing~~, Boy, et al., 2024) represents a new facet-based ~~numerical simulations combined with high-resolution DEM data~~ waveform simulation approach to ~~simulate~~slope correction. When applied to Sentinel-3 ~~UnFocused~~-UF-SAR (Unfocused Synthetic Aperture Radar~~ (UF-SAR) waveforms. This approach was found to reduce slope-related errors and yield more precise ice sheet elevation measurements than prior methods.~~) data over the Antarctic ice sheet, the AMPLI method reduced the median elevation bias and median absolute deviation relative to ICESat-2 ATL06 by 18% and 51%, respectively, compared to the ESA Sentinel-3 Land Ice Thematic Product, which uses a slope-based approach. In areas with sloped terrain (>0.5 °), improvements reached up to 83% and 90%.

Formatted: Body Text

Geophysical and Instrumental Corrections

Before use, measurements need to be corrected for both geophysical and instrumental factors. These include accounting for the distance between the antenna and satellite centre of mass, dry and wet troposphere delays, ionospheric delays, and variations in the solid Earth, ocean loading, and polar tide (Quartly~~, Nencioli, Raynal, Bonnefond, Nilo Garcia, Garcia-Mondéjar, Flores de la Cruz, Crétaux, Taburet, Frery, Cancet, et al.,~~ et al., 2020). Additionally, ocean tide and inverse barometer corrections need to be applied over floating ice such as ice shelves, the latter of which accounts for changes in atmospheric pressure. Measurements of the satellite range are also impacted by the on-board clock (ultra-stable-oscillator) responsible for measuring the round-trip of the echo (Quartly~~, Nencioli, Raynal, Bonnefond, Nilo Garcia, Garcia-Mondéjar, Flores de la Cruz, Crétaux, Taburet, Frery, Cancet, et al.,~~ et al., 2020). Approaches for accounting for these various

corrections differ from mission to mission but commonly amount to adjustments of the order of several meters in total. For additional details relating to the corrections applied within the Sentinel-3 ground segment, the reader is referred to ~~(S3-MPC, 2022~~the Sentinel-3 SRAL Land User Handbook (Aublanc, Féménias, et al., 2024).

The Sentinel-3 Mission

This study focuses upon the performance of the Sentinel-3 radar altimeter. In this section, we therefore introduce the principal characteristics of the mission.

Mission and Instrument Overview

The EU's Copernicus programme ~~oversaw~~has overseen the design and production of a significant number of new satellites during the 2010s-2020s. One of these missions, Sentinel-3, has so far launched two satellites, the first of which, Sentinel-3A, launched on 6 February 2016, followed by Sentinel-3B on 25 April 2018. Sentinel-3 was designed, in part, as a successor to the European Space Agency's (ESA) previous altimetry satellites, ERS-1, ERS-2, and Envisat, with the intention of transitioning to an operational programme, and securing a near-continuous ~30 year record of global altimetry data. During the lifetimes of Sentinel-3A and 3B, two further satellite launches are planned, Sentinel-3C and D, in order to sustain an unbroken observational record into the next decade. Sentinel-3 has an orbital period of 101 minutes such that after 385 complete revolutions (27 days), the ground-track is repeated to within 1 km. This orbital configuration yields ~~an across~~a track-to-track spacing of 0.94 °° longitude at the Equator (Quartly~~, Nencioli, Raynal, Bonnefond, Nilo Garcia, Garcia-Mondéjar, Flores de la Cruz, Crétaux, Taburet, Frery, Cancet,~~ et al., 2020). Both the 3A and 3B satellites orbit with a 98.65 °° inclination, thus providing coverage between 81.35°°S and 81.35°°N. The orbit is also configured to maintain a short-repeat sub-cycle, such that after 4 days the mission obtains quasi-global coverage, with a wider ~7 °° spacing of ground tracks at the equator (Quartly~~, Nencioli, Raynal, Bonnefond, Nilo Garcia, Garcia-Mondéjar, Flores de la Cruz, Crétaux, Taburet, Frery, Cancet,~~ et al., 2020). Driven by its mission objectives, Sentinel-3 operates in a lower inclination orbit and with a much smaller range window than CryoSat-2 (~92.03 °° and ~240 m in SAR (Synthetic Aperture Interferometric mode), respectively). The lower inclination orbit means that significantly more of the interior of the AIS is missed. However, as Sentinel-3 operates in SAR mode across the entire AIS (unlike CryoSat-2), much of the interior of the ice sheet is for the first time mapped with a higher along-track resolution. Due to the smaller range~~-~~ window of ~60 m (EUMETSAT, 2017), however, it is not uncommon for Sentinel-3 to fail to capture the surface echo, especially across coastal regions of the ice sheet that exhibit complex topography. ~~Although Sentinel-3 has the capability to operate an open-loop tracker (first introduced on Jason-2) known as the Open-Loop Tracking Command (OLTC), early assessments over the ice sheets' margins that were conducted during the Sentinel-3A commissioning phase led to the decision to favour closed-loop tracking over the ice sheets (Quartly, Nencioli, Raynal, Bonnefond, Nilo Garcia, Garcia-Mondéjar, Flores de la Cruz, Crétaux, Taburet, Frery, Cancet, et al., 2020).~~

During routine operations, Sentinel-3 operates nominally in closed-loop tracking mode across the ice sheets, thus mirroring the approach implemented on many previous altimeters, such as Envisat and CryoSat-2. Although the satellite was equipped with open-loop tracking capabilities from launch, and indeed this was activated during the commissioning phase of Sentinel-3A, subsequent analysis indicated that the Open-Loop Tracking Command (OLTC) tables were not sufficiently precise over the steep Greenland and Antarctica ice sheet margins to satisfactorily track the complex ice surface (SentiWiki, n.d.). Recently, however, several target areas have again been acquired with open loop tracking, for the purposes of re-evaluating and improving open loop tracking over ice sheets. Notably, the OLTC tables are now informed by the high resolution REMA and ArcticDEM DEMs, with the aim to overcome the limitations encountered during commissioning.

The primary altimetry instrument on board Sentinel-3, SRAL (Synthetic Aperture Radar Altimeter), is a Ku-band SAR altimeter, which ~~provides measurements~~ operates with a ~~resolution of~~ delay-Doppler beam-limited footprint of ~300 m along-track by ~~1.6~~18.2 km across-track. The across-track resolution of measurements is further constrained by the duration of the radar pulse, to ~1.6-2 km, depending upon surface topography ~~(Quartly, Nencioli, Raynal, Bonnefond, Nilo Garcia, Garcia-Mondéjar, Flores de la Cruz, Crétaux, Taburet, Frery, Cancet~~((Donlon, Berruti, Buongiorno, et al., ~~2020~~2012). The use of unfocused Synthetic Aperture Radar (SAR; also referred to as Delay-Doppler) processing (Love, 1985), allows the motion of the satellite relative to Earth's surface to be exploited, to deliver a four-fold improvement in the along-track resolution compared to traditional low resolution altimeters which are pulse-limited along track. Specifically, SRAL emits patterns of 64 coherent Ku-band pulses in a burst (i.e. with a high Pulse Repetition Frequency of 17.825 kHz), surrounded by 2 C-Band pulses (Donlon, Berruti, Mecklenberg, et al., 2012). A fast Fourier transform is then applied to the returned echoes in order to partition the received power into 64 "Doppler strips" along-track, and thus increase the instrument resolution to ~300 m along-track. Moreover, as a given Doppler strip is seen in the radar footprint multiple times, different looks of the same Doppler strip can be "stacked" in order to reduce the impact of radar speckle; a process that is referred to as multi-looking. While the concept of SAR processing has been applied within the context of radar imagers since the 1950s (Love, 1985) and has seen extensive application in previous satellite missions (Curlander & McDonough, 1991; Kovaly, 1976; Rosen et al., 2000), SAR processing has only recently been utilised by Earth-orbiting altimeters with the launch of CryoSat-2. This innovation has represented an important advance in polar Earth Observation, allowing smaller-scale features across ice sheets and sea ice to be resolved (Raney, 1998; Tilling et al., 2015). Accompanying SRAL, Sentinel-3 also carries a microwave radiometer (MWR), Sea and Land Surface Temperature Radiometer (SLSTR) and an Ocean and Land Colour Imager (OLCI) (Clerc, Donlon, Borde, Lamquin, Hunt, Smith, McMillan, Mittaz, Woolliams, Hammond, & others, 2020).

Data

The objective of this study is to provide a detailed assessment of the impact of surface topography on the performance of SRAL across the AIS. For the purposes of this study, we therefore analysed one complete cycle of data acquired by both Sentinel-3A and Sentinel-3B. Specifically, we selected cycle 54 for S3A and cycle 35 for S3B, which were acquired over the periods 15th January to 11th February 2020 and 25th January to 22nd February 2020, respectively. ~~We used the enhanced, baseline 4, non-time-critical, S2_2_LAN___ product, which was downloaded from the Copernicus Open Access Hub (https://scihub.copernicus.eu/dhus/#/home), and represented the latest product release at the time of the study.~~As our primary dataset, we used the Sentinel-3 Hydro-Cryo Altimetry Thematic Baseline Collection 005 Land Ice product (S3A_SR_2_LAN_LI and S3B_SR_2_LAN_LI; available at https://dataspace.copernicus.eu/). This product builds on the previous, unified BC-004 "Land Product", with a specific land ice chain that makes up one of three new families of “Thematic Products” (Aublanc et al., 2025). The BC-005 land ice product includes a number of dedicated ice sheet processing algorithms, the most notable of which involves artificially extending the range dimension of the delay-Doppler stack during Level-1 range migration and multilooking, in order to better preserve backscattered energy in the final waveform, particularly over the ice sheet margins (Aublanc et al., 2018; Aublanc et al., 2025). Further details relating to the thematic product can be found in the Sentinel-3 SRAL Land User Handbook (Aublanc, Féménias, et al., 2024). Additionally, for comparison purposes, we also utilise the BC-004 version product over the same cycles (also available at https://dataspace.copernicus.eu/)

In order to investigate the performance of Sentinel-3, we used the 100 m resolution, version-2 REMA (Reference Elevation Model of Antarctica) mosaic (I. Howat et al., 2018). REMA is a high-resolution DEM covering nearly 98% of Antarctica, which has been used for a range of cryospheric applications (Chartrand & Howat, 2020; Liu et al., 2023; Zinck et al., 2023). REMA was created by applying stereophotogrammetric techniques to submeter resolution commercial optical satellite imagery, including data from Maxar, WorldView-1, WorldView-2, and WorldView-3, as well as a small number of acquisitions made by GeoEye-1 (I. M. Howat et al., 2019). To form the mosaiced product, individual DEMs were registered to satellite altimetry measurements from CryoSat-2 and ICESat, leading to an estimated absolute uncertainty of less than 1 m, and relative uncertainties of the order of decimeters (I. M. Howat et al., 2019). ~~In order to improve computational efficiency when performing assessments at the ice sheet scale, we resampled the 100 m REMA mosaic to 200 m using nearest-neighbour interpolation~~For the purposes of this study, we selected REMA over other DEMs, such as the ICESat-2-derived gridded ATL14 product (Smith et al., 2021), as it is generated from stereoscopic techniques, and thereby provides a high-resolution, inherently two-dimensional product with minimal gaps. In contrast, the ATL14 product includes interpolation between ICESat-2 tracks, particularly as track-to-track spacing increases away from the poles (Smith, 2021), which makes it less well suited to constraining small-scale topographic characteristics, such as footprint-scale surface roughness.

Methodology

In this study, our aim is to assess and better understand the performance of the S3 altimeter over a variety of topographic regimes. To achieve this, we firstly use REMA to generate new ice sheet wide estimates of surface slope and roughness. We then performed three different sets of analysis (1) an ~~assessment of the extent to which the placement of the S3 range window successfully captures the point of closest approach on the illuminated ice surface, (2) an~~ evaluation of the extent to which the onboard tracker's placement of the range window and subsequent ~~L1~~ processing maximises the proportion of the illuminated topography that contributes to each waveform (i.e. that is captured by the range window), (2) an assessment of the extent to which the placement of the range window successfully captures the point of closest approach on the illuminated ice surface, and (3) quantification of the degree of correlation between along-track sequences of echoes. ~~The first~~The first analysis is designed to provide a first assessment of the effectiveness of the altimeter in adequately tracking the underlying topographic surface. The second analysis is designed to evaluate the assumption – which is inherent to most L2 processing schemes – that the waveform leading edge originates from the closest point within the beam footprint; and then to investigate how the validity of this assumption varies with increasing topographic complexity. ~~The second analysis is designed to provide a first assessment of the effectiveness of the altimeter in adequately tracking the underlying topographic surface.~~ The third analysis evaluates the extent to which the complexity of the topographic surface – characterised by slope and roughness – causes decorrelation in successive delay-Doppler echoes. In the following sections, we outline the methodology used for each of these analyses, in turn.

Ice Sheet Surface Slope and Roughness from REMA

To understand the impact of ice sheet surface topography on the performance of the Sentinel-3 altimeter, we used the REMA dataset to compute continent-wide estimates of ice sheet surface slope and roughness. Within the context of this study, these parameters are important because they can affect (1) the ability of the altimeter to track the ice sheet surface, (2) the effectiveness of approaches to derive the ~~Level-1b (L1b)~~ waveform, and (3) the degree of correlation between sequences of waveforms acquired along the satellite track.

We generated our own slope and roughness maps using REMA in order to tailor the algorithms used to fit with the objectives of this study. Although there exist several easy-to-apply methodologies for calculating slope from DEMs (Horn & Schunck, 1981; Zevenbergen & Thorne, 1987), common approaches for calculating roughness such as the Terrain Ruggedness Index (TRI) (Riley et al., 1999~~) and),~~ the Topographic Position Index (TPI) and Roughness (Wilson et al., 2007~~),~~ do not fit our use-case, despite extensive application in GIS (Geographic Information System) programs and packages such as GRASS, ArcGIS, and GDAL (used by QGIS). This is because these methods use the local variance in elevation as a measure of roughness, but neglect to account for topographic slope.

Instead, they calculate the differences between a pixel and its immediate neighbours, which would, for example, return a non-zero roughness value over a perfectly smooth plane inclined at an angle. ~~As such, values determined for slope and roughness calculated in this way encode each other via complex, non-linear interactions. To address this, we therefore calculate roughness independently of slope, by taking the dispersion of orthogonal residuals from a plane fitted through a given DEM point and its neighbours. To do so, we use Singular Value Decomposition (SVD), which we apply using a sliding-window approach. Specifically, we use a 5x5 pixel (1000x1000 m) window,~~Consequently, the roughness values produced by these methods are dependent on slope, making it difficult to separately assess their individual contributions to topographic variation. More advanced metrics such as the Vector Ruggedness Measure (VRM) (Sappington et al., 2007) attempt to address this through calculating the dispersion of local surface normals, but (1) do not explicitly decouple slope from the roughness calculation, and (2) express roughness as a unitless 0–1 value, which neglects recording useful elevation amplitude information. To address these prior limitations in slope-roughness coupling explicitly, we therefore calculate roughness by quantifying the dispersion of orthogonal residuals from a best-fit plane, implemented using Singular Value Decomposition (SVD), and applied over a sliding-window. In addition to eliminating any artificial correlation between slope and roughness that is introduced by other methods, this approach also provides a more accurate measure of slope than commonly used approximations such as Horn's method (Horn & Schunck, 1981) by explicitly fitting a plane, whilst also allowing for flexible window sizes beyond the 3x3 pixel constraint inherent to those approaches. To fit the plane, SVD was chosen, rather than a least-squares (LS) approach, as SVD fits a plane by minimising orthogonal residuals, whereas LS minimises residuals in the vertical (z) direction. This, we believe, makes SVD more suitable for fitting surfaces over complex terrain, where minimising the true geometric (orthogonal) distance is expected to yield a more representative estimate of the surface slope. Furthermore, SVD directly returns the normal vector to the fitted plane during the fitting process, with LS otherwise requiring a separate, additional calculation. For the window size, we used 9x9 pixels (900x900 m), with slope and roughness parameters only computed where more than half of the pixels within a window contained a valid elevation measurement. The window size was chosen to be broadly consistent with the size of the pulse ~~limited footprint and to minimise the impact of missing data. To obtain slope and roughness values, we first centre the data within each window by subtracting the means of their x, y and z coordinates. We then apply SVD in order to decompose the centre points in each window into three distinct matrices (Equation [eq:SVD]), and take the left singular matrix, U, which contains three orthogonal unit vectors describing a plane of best fit:~~-limited footprint and to minimise the impact of missing data.

~~$$M = U\Sigma V^T$$~~

~~Here, $\mathbf{M}$ the is original matrix that we want to decompose, $\mathbf{U}$ is the left singular matrix, $\mathbf{\Sigma}$ is a diagonal matrix containing singular eigenvalues, $\mathbf{V}$ is the right singular matrix, and T is the matrix transpose operator.~~

~~By calculating the partial derivatives $\frac{dz}{dx}$ and $\frac{dz}{dy}$, we determine the resulting gradient and hence the surface slope. Roughness is then directly computed based on the standard deviation of the orthogonal residuals, which are calculated by taking the dot product of the centred elevation points with the normal vector to the plane. Since we define roughness to be one standard deviation of the orthogonal residuals, it is important to note that the values stated in the text should be interpreted as characterising 68% of the roughness variance, and not the peak-to-trough elevation difference, or amplitude, of the local topographic variation.~~

To obtain slope and roughness values we first construct a matrix $\mathbf{M} \in \mathbb{R}^{n\times 3}$, containing the n mean-centered 100 m resolution REMA coordinates (x, y, z) within each window (Equation [eq:M_matrix]). We then apply SVD to this matrix, as defined in Equation [eq:SVD], which decomposes $\mathbf{M}$ into the product of three matrices: an orthogonal matrix $\mathbf{U}$ containing the left singular vectors, a diagonal matrix $\mathbf{\Sigma}$ containing the singular values in decreasing order, and an orthogonal matrix $\mathbf{V}$ whose columns are the right singular vectors. The right singular vector corresponding to the smallest singular value - i.e., the last row of $\mathbf{V}^T$ - defines the unit normal vector $\mathbf{n} = [n_x, n_y, n_z]$ of the best-fit plane through the points in the window. The surface slope is then derived from the gradient of the fitted plane, given by the partial derivatives $\frac{\partial z}{\partial x}$ and $\frac{\partial z}{\partial y}$ (Equation [eq:gradients]), with a final, singular slope value s computed by taking the Euclidean norm of the two directional gradients and converting to degrees. This yields the local surface slope angle, independent of orientation (Equation [eq:slope]). Roughness r is calculated as the minimum-to-maximum range of the orthogonal residuals, obtained by taking the dot product of each centered point with the plane normal, where $\mathbf{m}_i$ is the i-th row of $\mathbf{M}$ (Equation [eq:roughness]). To obtain single slope and roughness values for each record, we then take the mean of the pixel values contained within the corresponding beam-limited footprints.

$$\mathbf{M} = \begin{bmatrix} x_1 - \bar{x} & y_1 - \bar{y} & z_1 - \bar{z} \\ \vdots & \vdots & \vdots \\ x_n - \bar{x} & y_n - \bar{y} & z_n - \bar{z} \end{bmatrix}$$

$$\mathbf{M} = \mathbf{U}\mathbf{\Sigma}\mathbf{V}^T$$

$$a = -\frac{n_x}{n_z}, \quad b = -\frac{n_y}{n_z}$$

$$s = \arctan\left(\sqrt{a^2 + b^2}\right) \cdot \left(\frac{180}{\pi}\right)$$

$$r = \max_i(\mathbf{m}_i \cdot \mathbf{n}) - \min_i(\mathbf{m}_i \cdot \mathbf{n})$$

To facilitate comparison with established methods, we also generate a slope map using Horn's method (Horn & Schunck, 1981), applied to the same 100 m resolution REMA dataset. Since Horn's method uses a 3x3 pixel window (300x300 m), we re-compute our slope map using the same window size for a fair comparison. Similarly, we compute

roughness maps using TRI and our method, again using a 3x3 pixel window to ensure consistency with TRI. Here, TRI was chosen over alternatives such as TPI and Roughness due to its more extensive prior application in terrain analysis (Trevisani et al., 2023).

Window Placement Optimisation

Prior to performing a detailed assessment of the range window placement relative to the point of closest approach (Sect. 4.3), we first investigated more broadly the extent to which the placement of the range window maximises the capture of the topographic surface illuminated by the beam-limited footprint. Our motivation for this analysis is grounded on the principle that maximising the amount of information captured is beneficial for a range of present and future use cases. Specifically, whilst it is clear that current non-interferometric processing methods largely rely on information extracted from the leading edge of the waveform, it is likely that future advances in retrieval algorithms may allow full-waveform retrievals. Thus, there is benefit to assessing how the size and placement of the range window can be optimized in order to capture as much of the illuminated surface as possible.

To perform this analysis in practice, for each echo within our chosen cycles (comprising a total of 8,~~124,014~~125,872 records), we computed the proportion of DEM points within the beam-limited footprint that fell above, within and below the ~~~~60 m range window, where the beam-limited footprint was defined with dimensions of 18,200 and 300 m in the across and along-track directions, respectively.

Because over complex topography, the range of elevations within the beam-limited footprint exceeds that spanned by the range window, it is, in places, impossible for the range window to entirely capture the illuminated topographic surface. To account for this, we therefore also ~~compute~~computed the hypothetical positioning of the range window that ~~maximises~~would have maximised the capture of topography, together with the associated percentage of the illuminated surface that could be captured within it. This ~~is~~was done by iteratively moving the range window by 1-meter increments in range, to determine the position that ~~maximises~~maximised topographic capture. Having located the optimal range window ~~location~~placement, we were then able to quantify the possible increase in the proportion of the surface captured, which could be realised with a refined range window placement~~. This is computed as the ratio of actual to maximal topographic capture~~, whilst respecting the inherent limitations imposed by the 60 m range window size. This was assessed by computing the ratio of actual to maximal topographic capture. Finally, we also computed the optimal range window position – and thus the maximum possible topographic capture – that could be achieved for varying-sized range windows; specifically: 60 m, 120 m, 180 m, 300 m, and 360 m. This allowed us to explore the extent to which an increased range window size would, in principle, yield greater capture of the illuminated topographic surface, with a view to improving our broader understanding within the context of other current and future satellite altimetry missions overflying Antarctica.

Formatted: Body Text

Capture of the Point of Closest Approach

Following the methodology presented in Sect. 4.1, we also ~~perform~~performed a similar assessment, which ~~is~~ focused specifically on evaluating the window position relative to the point of closest approach. This is motivated by the fact that, within conventional L2 altimetry processing chains, an assumption is made that the echoing point (the so-called POCA) lies within the intersection of the range window and the beam-limited footprint (class 2 in Fig. 1~~).~~); and thus that the return from the POCA location corresponds to the range to the waveform leading edge. However, around the complex topography of the ice sheet margin, this assumption does not always hold, particularly for Sentinel-3, due to its relatively small (~60 m) range window. In regions of high slope, the POCA may lie outside the beam-limited footprint, meaning that any backscattered energy will be highly attenuated by the antenna gain pattern, whereas in regions of rugged (highly variable) topography, the POCA may lie at an elevation not captured by the range window. With the availability of new, high-resolution DEMs such as REMA, comes the opportunity to explicitly assess the extent to which the echoing point lies within the intersection of the beam-limited footprint and the range window, and hence the extent to which this common assumption in L2 processing chains is satisfied. Furthermore, by comparing success and failure at the ice sheet scale to covariates such as surface roughness and slope, ~~it is possible~~we aim to assess how performance is affected by topographic complexity. For all S3A and S3B echoes within our chosen cycles, we therefore classified where the identified POCA location lay relative to the positioning of the S3 range window. The acquisition geometry and related definition of the POCA classes are shown in Fig. 1.

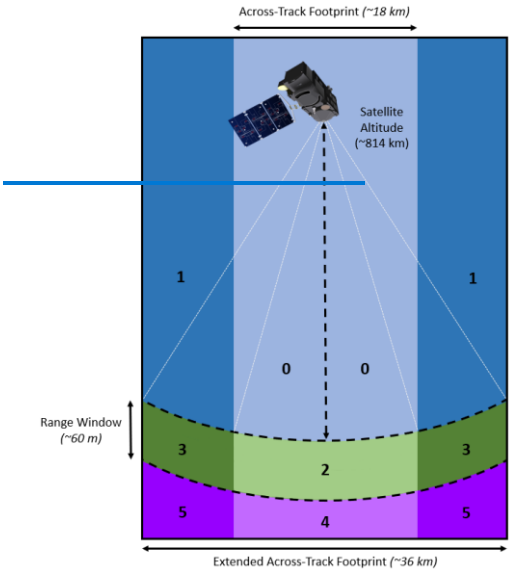

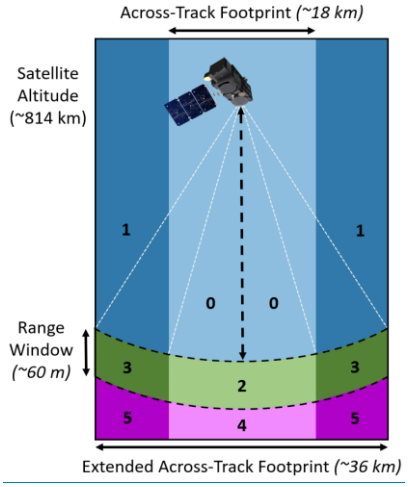

Illustration of the Sentinel-3 SAR altimetry acquisition geometry in the across-track plane (satellite flying into the page), showing the classification scheme used to categorise each ~~echo~~acquisition according to the location of the POCA relative to the positioning of the ~~L1b~~ range window. Above the range window is shaded in blue (classes 0, 1), below in magenta (classes 3, 4), and within the range window in green (classes 2, 3). Darker shades of each colour represent locations outside of the across-track beamwidth.

Within this assessment, we performed two sets of analyses. First, we evaluated the positioning of the range window relative to the POCA location that was defined within the standard L2 product. ~~This allowed~~Here, slope correction - and consequently the determination of the location of the POCA within the SAR footprint - is performed via a slope-based approach using a surface slope model precomputed from DEMs over Antarctica and Greenland (Aublanc, Féménias, et al., 2024; Helm et al., 2014; IPF, 2024). This analysis allows us to determine the extent to which the slope correction applied within the L2 processing chain ~~identified~~identifies an echoing point that ~~was~~is consistent with the actual acquisition geometry (i.e. ~~tay~~lies within both the beam-limited footprint and the range window~~).~~); in other words, whether the subsequent elevation measurement derived by retracking the waveform can reasonably be attributed to the assigned POCA location. Secondly, we performed the same evaluation, but for a POCA location that we determined, independently, by minimising the range between the ice surface and the altimeter, using the REMA DEM. This procedure is analogous to the methodology underlying the point-based relocation approach ~~of~~first introduced by (Roemer et al., 2007), albeit ~~we extend the~~using an extended search region to include instances where the POCA lies beyond the ~~3dB~~3 dB beamwidth (Fig. 1). ~~As such, we~~We refer to ~~this~~ the identified surface location as the ~~Roemer-derived POCA. This analysis is designed to evaluate~~REMA-derived POCA. It is important to note that although the underlying algorithm is similar, the purpose of this analysis is not to perform a slope correction (i.e. the intention is not to derive relocated elevation measurements as part of a standard L2 processing chain). Rather it is simply to determine the location of the closest surface point to the satellite (as determined by REMA), thereby allowing us to identify the extent to which the ~~POCA is actually captured within the 3-D window defined by the~~positioned range window ~~and the antenna 3dB beamwidth~~captures this POCA location.

To perform these analyses, we first located the range window relative to the ice surface for each of the ~8 million altimeter records considered in this study, and then compared it to the two POCA locations. Specifically, we adjusted the range to the nominal tracking point (defined for S3 as the 43rd bin in the range window) according to the geophysical and instrument corrections supplied within the product, to account for path delays due to dry tropospheric, wet tropospheric and ionospheric effects; tidal and atmospheric pressure induced variations, and the instrument Centre of Gravity (COG) correction. As all of these corrections are supplied at 1 Hz, we used linear interpolation to match these to the native 20 Hz frequency of the range and elevation measurements. Finally, the dimension of the range window (128 bins) was used to locate the range to the start and end of the window for each record. To reference the range window to the DEM elevation, we then subtracted the satellite altitude.

Next, we computed the geographic coordinates and elevation of the POCA for both the L2 and ~~Roemer~~REMA derivations, in order to classify them according to their position relative to the range window (Fig. 1). For the L2 evaluation, the geographic coordinates ~~(x,y)~~(x, y) were simply taken from the product. For the surface elevation ~~(z)~~(z) at the L2 POCA, we chose to extract the elevation at this location from the closest REMA pixel, rather than use

the elevation within the altimeter product, because the purpose was simply to compare the range window to a reference surface, rather than interpret the altimeter elevation itself. This approach therefore avoided missing data in the L2 product. We ~~chose~~selected the ~~closest~~nearest REMA point, rather than ~~employing~~applying a more complex interpolation method, as the ~~DEM~~100 m posting ~~of 200 m~~ is ~~smaller~~already finer than the altimeter resolution ~~of the altimeter measurements~~ (~1600 x 300 m). In this regard, our aim is a coarse-scale classification of the POCA location relative to the range window, rather than the derivation of relocated elevation measurements themselves, and so a more detailed interpolation was unnecessary. For the ~~Roemer~~REMA derivation of the POCA, we computed the echoing point location based upon the DEM pixel that minimised the range between the satellite and the ice surface.

Along-track Decorrelation of Echoes

Finally, we ~~explored~~explore the extent to which ice sheet surface topography causes decorrelation in sequences of SAR waveforms, as they are acquired along the satellite track. This analysis extends the work of McMillan et al. (~~2019~~2021), to investigate the rate at which waveforms decorrelate in space (along-track), and the extent to which this is governed by the topographic characteristics (slope and roughness) of the surface. More specifically, we ~~calculated~~calculate (1) correlations between adjacent pairs of waveforms aligned in range, and (2) correlations between ~~a seed~~every waveform and ~~its~~the 50 subsequent ~~50 records~~waveforms along-track (spanning a distance of ~~~~~15 km), also aligned in range. The latter assessment ~~allowed~~allows us to quantify the rate at which waveforms decorrelate in space, spanning distances that are representative of those over which altimetry measurements are commonly aggregated, for example when computing rates of surface elevation change. The overall intent of this analysis is to assess how the topographic characteristics of present day ice sheets influences the spatial decorrelation of SAR waveforms, which is motivated by the hypothesis that topographically complex areas drive a more rapid decline in correlation between a given waveform and those acquired subsequently along-track. At a practical level, understanding this relationship is of interest, as decorrelation characteristics may influence the effectiveness of combining information from waveforms acquired over different spatial scales. For example, surfaces with greater slope or roughness may induce more variability between nearby waveforms, which may complicate the aggregation of elevations derived from spatially distributed waveforms, for the purposes of computing rates of surface elevation change. Ultimately, by examining these relationships, we aim to provide initial insights into how surface morphology impacts waveform structure, which can help to inform future work towards improved strategies for processing SAR altimetry data in areas of complex topography.

To ~~do this~~determine the correlation between any two waveforms, we first normalise the power of each to be between 0 and 1. To avoid cases where a given waveform ~~and reject any waveform whose~~was excessively noisy, correlations were not computed when the mean power ~~does~~did not exceed the estimated thermal noise by more than 0.15, with thermal noise computed as the mean of the 6 lowest-value waveform samples (Helm et al., 2014; McMillan et al., 2019). ~~To compute the correlation of any given waveform~~

~~pair~~Next, we ~~first align~~aligned both waveforms according to their centres of gravity (COG) ~~(~~according to Equation [eq:COG], where N is the number of waveform bins (128), and P_n is the power at bin n.~~),~~ Following this, we retained only the overlapping region of the two waveforms, removing any bins that ~~lie beyond the bounds of the original waveform samples.~~ did not intersect.

In order to focus on correlating the principal surface response, rather than peripheral signals and waveform noise, we ~~mask~~masked the aligned waveforms by removing peripheral bins from each side of the range window, until a bin with power above 0.15 (chosen for consistency with the previous noise detection ~~and visual inspection) is~~) was found in either waveform. If the clipped waveforms ~~have~~had at least 16 bins remaining, we then ~~compute~~computed the Pearson correlation coefficient using the pairs of normalised waveform samples. A minimum threshold of 16 bins was chosen as a reasonable lower bound for what constitutes a valid response, based upon an assessment of the waveforms that passed the L2 ice quality checks, which retained a mean COG width of 27.1 bins and standard deviation of 10.2.

$$\mathrm{COG} = \frac{\sum_{n=1}^{N} n\, P_n^2}{\sum_{n=1}^{N} P_n^2}$$

~~Here, N is the number of waveform bins (128), and P_n.~~ Next, ~~is the power at bin n.~~

~~We repeat this process~~ for each waveform, we computed its Pearson correlation with each of the subsequent 50 waveforms ~~in the sequence, in order to derive~~along-track, yielding a series of correlation values relative to the ~~seed~~initial waveform. ~~Then, where~~If more than 25 correlation values ~~are returned~~were available, we ~~fit~~fitted a linear regression to estimate the rate of change in correlation as a function of along-track distance ~~along-track. We constrain~~. To ensure comparability between all regressions, we explicitly included a correlation value of 1 at $d = 0$, representing the waveform's self-correlation, and constrained the regression to ~~be 1 at its initial value, and then, using the correlation gradient, compute the change in the~~ pass through this point, such that the fitted line followed Equation [eq:correlation_decay], where d is the number of records along-track, $R(d)$ is the Pearson correlation coefficient, and m is the along-track rate of change in correlation, per 20 Hz measurement. This slope captures the linear decay in correlation from the initial waveform to increasingly distant waveforms along-track, computed over 50 subsequent records (~15 km).

$$R(d) = 1 + m \cdot d$$

Using the fitted slope, we computed the change in correlation at record 50. This provides a more stable estimate of the change in waveform correlation after 15 km, which is not solely dependent upon the initial and 50th records. Based on this approach, a value of 0 ~~indicates~~indicates that waveforms 15 km away are perfectly correlated, whilst a value of -1 corresponds to waveforms that are fully decorrelated (R=0) after 15 km. Values less than -1 indicate that waveforms are anti-correlated after 15 km; i.e. an increase in power in one waveform corresponds to a decrease in power in the other. This is likely to reflect

Formatted: First Paragraph

limitations in the COG alignment of complex waveforms (e.g. correlating a single peak with a double peak waveform) and so we focus our analysis on correlation values between -1 and 0.

To analyse the effect of surface topography on these metrics, we then derived estimates of across-track surface slope and roughness for a 1-D across-track profile approximating the beam footprint of each record, using a 2-D version of the SVD approach described in Sect. 4.1. We intentionally focused this assessment of waveform similarity on across track slope and roughness, because the anisotropic shape of the delay-doppler footprint means that these parameters in the across-track direction are most likely to have the largest influence on waveform shape.

Results

Ice Sheet Slope and Roughness from REMA

First, we analysed the surface slope and roughness characteristics of the Antarctic Ice Sheet, based upon our newly-derived REMA datasets (Fig. 2). Our new surface slope map shows well-established patterns of very low (< 0.~~03 °)~~1 °) surface slope at the ice divides and the floating ice shelves, with steeper slopes prevailing towards the grounded ice sheet margin. Overall, we find that ~~57.4~~76.9% and ~~90~~89.1% of the ice sheet have a surface slope below 0.~~1~~5 and 1.0~~.5 °,~~ °, respectively. In addition to the large-scale characteristics of slope, our new map also shows detailed signatures of topography and ice dynamics, such as the flow of ice across the Ross and Filchner-Ronne Ice Shelves from their upstream tributaries, and the numerous ice rises that lie close to these ice shelves' grounding lines. Turning to ice sheet surface roughness, we find that that ~~64.9~~62.4% and ~~89.5~~76.1% of the ice sheet have a ~~1-standard deviation~~ surface roughness below 0.~~1~~5 and 1.0~~.5~~ m, respectively, with lower roughness persisting mostly within the interior of the ice sheet. Of particular note are the clear signatures of mega dune fields in East Antarctica, which typically have roughness of the order of ~1 m and the patterns associated with ice flow across the Ross and Filchner-Ronne Ice Shelves. In broad terms, the interior of West Antarctica is rougher than East Antarctica and, as with surface slope, there is a general trend to increasing roughness towards the ice margin, with surface roughness often reaching several meters close to the coast.

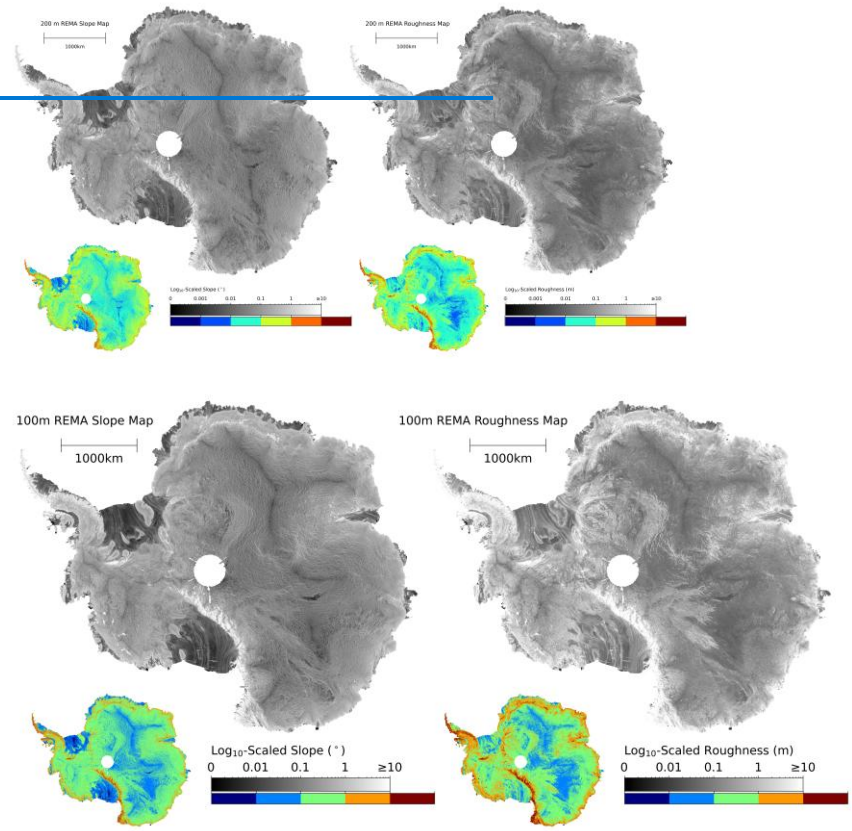

5 km resolution, log_{10}-scaled slope and roughness maps of Antarctica generated using ~~200~~100 m resolution REMA and the Singular Value Decomposition techniques outlined in Sect. 4.1. The coloured inset maps show discretely binned versions of these datasets, to aid the visualisation of broader scale patterns.

We find that the ice sheet as a whole has a median slope and roughness of 0.~~070 °~~192 ° and of 0.~~061~~297 m, respectively. We characterise the degree of spatial variability of each parameter across the ice sheet by computing the median absolute deviation, which is 0.~~044 °~~134 ° and 0.~~045~~219 m for slope and roughness, respectively. To explore in more detail the relationship between surface slope and roughness, we plot their joint and marginal distributions (Fig. 3), which shows a positive relationship between the two variables. Taking the Pearson correlation coefficient, we obtain a value of 0.~~730 (p-value < 0.01);~~808, indicating that the two values are significantly linearly correlated. Because we have calculated roughness via the dispersion of orthogonal residuals to the fitted slope, the two variables remain algorithmically independent. Therefore, this correlation reflects a

physical relationship between these topographic glaciological parameters, indicating that areas with higher surface slope are also more likely to exhibit higher surface roughness. Broadly, we find that roughness increases by ~~1.~~4.38 m per degree increase in surface slope.

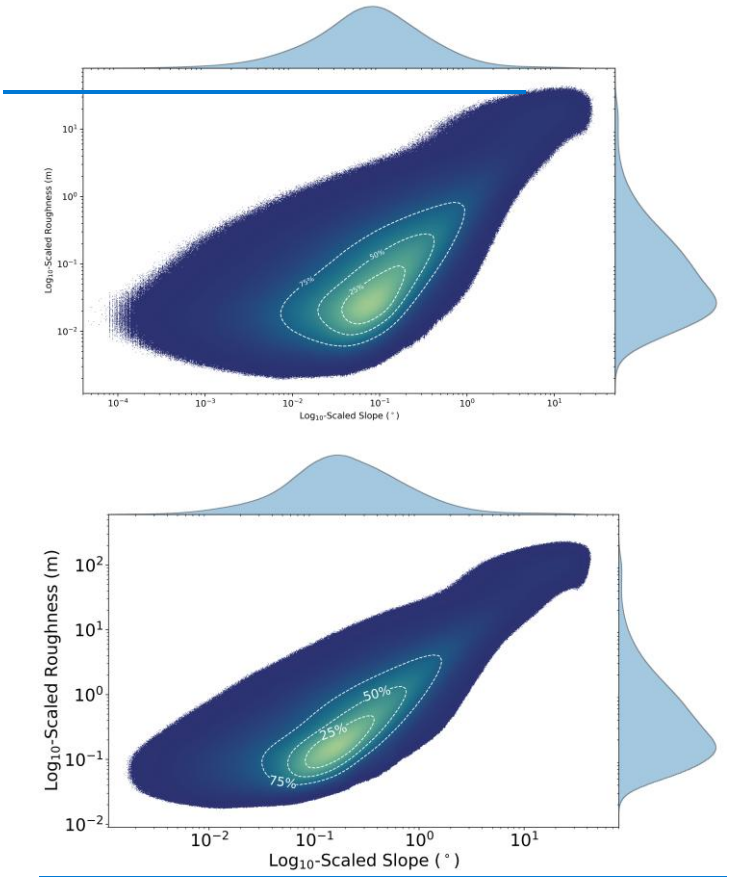

Log_{10}-binned joint and marginal distributions of slope and roughness across Antarctica. The joint distribution is displayed as a density plot, with lighter colours indicating a higher density of measurements, and the contours bounding 25%, 50%, and 75% of the data.

As outlined in Sect. 4.1, we also compare our slope estimates to those calculated using Horn's method (Horn & Schunck, 1981). This comparison includes both the slope map shown in Fig. 3, which was generated using a 9x9 pixel window, and an alternative version that used a window size of 3x3 pixels (300x300 m) to match the window dimensions of Horn's method (Fig. 4 a). The three results show very close agreement, all attaining the

same Gaussian shape on a $\log_{10}$ scale. Specifically, the slope maps derived using Horn's method and our SVD-based approach (both with 3x3 pixel windows) yield median values of 0.199 ° and 0.198 °, respectively, and identical MADs of 0.138 °. The difference between our 3x3 and 9x9 pixel implementations is also negligible (median difference < 0.01 °). These results indicate that, when assessed at the scale of the entire ice sheet, and at a resolution of 100 m, neither the choice of window size (3x3 versus 9x9) nor the underlying slope estimation method has a significant impact. It is important to note, however, that the SVD approach is more flexible in offering a generalised solution that can be applied to variable and irregular window shapes, making it better suited for cases where a super-resolution DEM is used, or where slope is estimated over an anisotropic area, such as the 1-D window geometry utilised in Sect. 4.4.

Secondly, we performed a similar analysis for our SVD-derived roughness map (calculated using 3x3 pixel windows), comparing it with estimates made using a 9x9 pixel window, and using the Terrain Ruggedness Index (TRI) approach (Riley et al., 1999) (Fig. 4 b). Our method yields a median roughness of 0.03 m and a median absolute deviation of 0.0181 m for a 3x3 pixel window, and a median roughness of 0.297 m and median absolute deviation of 0.219 m for a 9x9 pixel window. For TRI, the corresponding values are 0.864 m and 0.592 m, respectively, indicating that our method produces consistently lower roughness values than TRI for both window sizes. The higher values produced by TRI likely reflect its dependency between slope and roughness, whereby steeper slopes inflate roughness estimates. To assess this, we computed the Pearson correlation coefficient between slope and roughness for both methods. We find a stronger correlation for TRI (0.947) than for our approach using the same 3x3 window (0.720), suggesting that our method is indeed more effective at reducing algorithmic slope-roughness correlation. Turning next to the choice of window size, we find that unlike for slope, the choice of window size has a substantial effect on roughness estimates, with the 3x3 window producing lower values than the 9x9 window (Fig. 4). This likely reflects the fact that an increased number of points in a larger window raises the likelihood of higher minimum-to-maximum variance relative to the fitted plane. Nonetheless, even with a 9x9 window, the distribution of roughness values is still lower for our method than for TRI. Finally, within the context of this study, it is important to note that it is primarily the variance in roughness that is analysed (through comparison to altimetry measurements) rather than the absolute roughness values themselves.

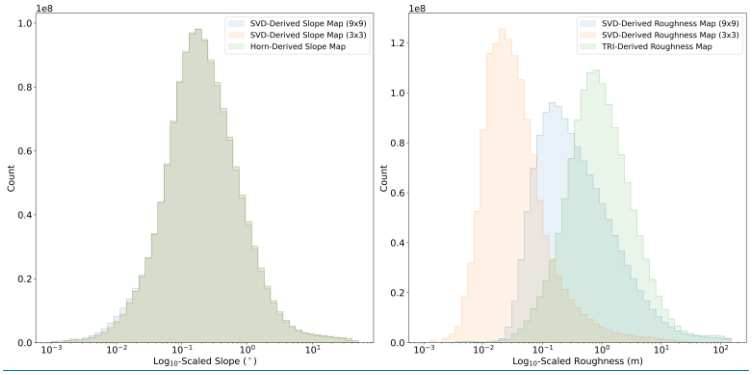

Comparison of slope and roughness estimates using different methods applied to the 100 m resolution REMA DEM. Panel a shows slope calculated using (1) Horn's method with a 3x3 pixel (300x300 m) window, (2) our SVD-based approach, calculated with a 3x3 pixel window for consistency with Horn's method, and (3) our SVD-based approach with a 9x9 pixel window. Panel b shows roughness computed using (1) TRI (3x3 pixel window), (2) our SVD-based approach using the same 3x3 pixel window size for consistency with TRI, and (3) our approach using a 9x9 pixel window.

Window Placement Optimisation

The S3 ~~L1b~~ product records backscattered energy over a range window of ~60 m. As such, there are areas of the AIS where the degree of topographic variance within the beam-limited footprint makes capturing the full topography within the range window impossible. Determining the locations and extent of these regions is of interest because it indicates where (1) waveforms are likely to be truncated or highly complex, (2) relocation errors may be prevalent, and (3) positioning of the range window will, ultimately, have a major impact upon ~~reliable~~ the reliability of retrievals of ice sheet elevation. ~~We~~By assessing the proportion of illuminated terrain that could be captured with an optimal placement of the 60 m range window (Sect. 4.2), we found that, for ~~23.7~~57.4% of recorded echoes, full (100%) topographic capture was impossible ~~within the 60 m range window, with this occurring~~. With optimal window placement, however, 83.5% of acquisitions would be able to acquire at least 80% of the topography illuminated by the beam-limited footprint. Failure to capture the full topography primarily occurs in coastal ~~areas that exhibit~~regions of the ice sheet with high topographic complexity (Fig. ~~4~~5 a~~).~~), and reflects a fundamental limit imposed by the 60 m size of the Sentinel-3 range window, rather than the onboard tracker implementation.

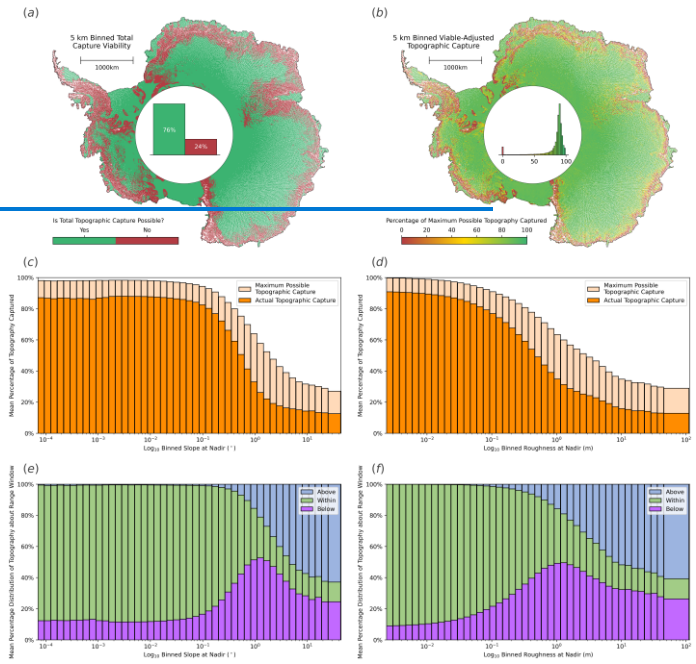
(a)
5 km Binned Total Capture Viability
1000km
76%
24%
Is Total Topographic Capture Possible?
Yes
No
(b)
5 km Binned Viable-Adjusted Topographic Capture
1000km
0
50
100
Percentage of Maximum Possible Topography Captured
0
20
40
60
80
100
(c)
Maximum Possible Topographic Capture
Actual Topographic Capture
Mean Percentage of Topography Captured
Log10 Binned Slope at Nadir (°)
(d)
Maximum Possible Topographic Capture
Actual Topographic Capture
Mean Percentage of Topography Captured
Log10 Binned Roughness at Nadir (m)
(e)
Above
Within
Below
Mean Percentage Distribution of Topography about Range Window
Log10 Binned Slope at Nadir (°)
(f)
Above
Within
Below
Mean Percentage Distribution of Topography about Range Window
Log10 Binned Roughness at Nadir (m)

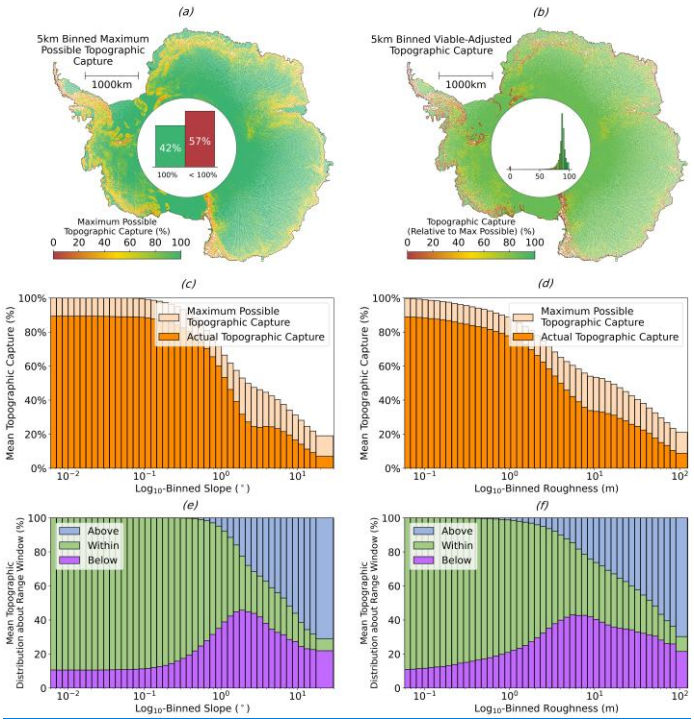

Assessment of the ability of the Sentinel-3 ~~L1b~~ range window to capture the full topographic surface within the beam-limited footprint. Panel a exhibits ~~where total topographic capture within~~the maximum possible percentage of topography (REMA; 100 m resolution) that can be captured with an optimal placement of the 60 m range window ~~is possible~~, binned to 5 km. The percentage of records where full (100%) topographic capture is, and is not, possible is shown within the bar graph in the pole hole. Panel b shows the percentage of ~~the maximum possible~~ topography that is captured by the current placement of the range window~~;~~ with respect to the maximum possible capture (panel a), binned to 5 km, with the corresponding distribution shown within the pole hole. A value of 0 indicates that the current placement of the range window entirely misses the ice surface, whereas a value of 100 indicates that the range window captures the maximum possible area of the illuminated surface~~.~~ (not necessarily 100% of the surface). Panels c and d show stacked bar charts representing the maximum percentage of topography within the satellite footprint that can be captured, and that which is currently captured, with respect to log_{10}-binned slope and roughness respectively. Panels e and f show stacked bar charts, indicating the distribution of REMA ~~nodes~~points within the illuminated beam-limited footprint that are above, within, and below the range window, with respect to log_{10}-binned slope and roughness.

~~To~~Next, to assess the performance of the current ~~L1b~~ window placement, we then computed the ratio of actual to maximal topographic capture for each record (Fig. ~~4~~5 b), where the latter was determined by calculating the maximum percentage of the illuminated surface that could have been captured with a refined placement of the range window (Sect. 4.2). At a practical level, this analysis was designed to assess the extent to which a greater proportion of the illuminated surface could be captured if refinements are made to the positioning of the range window. On average, across all records, the current window placement acquired a median of 89.~~7~~2% of the total possible topography that could be captured, with a median absolute deviation of ~~3.27~~2.47%. This demonstrates that, even over areas where full topographic capture is impossible, further refinement to the placement of the range window could allow a ~~larger~~greater proportion of the surface return to be recorded. ~~Notably~~

To assess the impact of recent changes made to the Level-1 processing, we also performed a similar analysis for the previous BC-004 product, which did not include extended window processing and waveform centering (Aublanc et al., 2025). Relative to BC-004, we find that although the percentage of possible capture is is broadly similar (< 1% difference) over the low slope interior of the ice sheet (< 1.0 ° slope), the BC-005 product performs substantially better (+7.6%) across the higher sloped margins (1.0-2.5 ° slope). Broadly similar behaviour is observed with respect to surface roughness, with < 1% difference and a +2.2% improvement for the latest product, in ~~2.20% of~~ regions where the surface roughness is < 5 m and 5-10 m, respectively. As such, this analysis allows suggests that the extended window processing and waveform centering has indeed improved data capture over high sloped terrain, where the along-track variation in tracker range during the SAR integration time is greatest.

In interpreting, and potentially acting on, this analysis of topographic capture, it is important to note that in some cases~~, the~~ where there is high topographic variability within the illuminated footprint ~~meant that,~~ positioning the range window to maximise topographic capture ~~resulted~~may result in the return from the POCA being missed. In these cases, there is a trade-off between maximising topographic capture and acquiring the reflection from the point of closest approach. For future missions that aim for full waveform retrievals~~,~~ (such as swath processing), this type of analysis can therefore help to inform decisions relating both to the size (i.e. the range ~~dimensions~~dimension) and the positioning (onboard tracking and L1 processing) of the range window. It should also be noted that ~~it is important~~ to resolve ~~an unambiguous~~the leading edge~~, which requires~~ clearly, the range window must record a ~~short~~brief period of no backscattered power ~~to be recorded prior to~~before the first return. This requires positioning of the upper boundary of the window slightly above the POCA to ensure the reliable detection of the waveform onset.

Comparing these results to our new slope and roughness datasets, we find that both the actual, and theoretical maximum, percentage of the illuminated topography that can be captured within the S3 range window decreases with increasing slope and roughness (Figs. ~~4~~5 c and d). Specifically, for $\log_{10}$-binned slope we observe ~~a reverse-sigmoidal trend,~~

~~with~~that ~90% of the illuminated surface is typically captured for slopes up to ~0.1 ~~°~~,°, followed by a ~~relatively rapid~~steady decline to ~~10-~~20-30% capture by the time slopes reach ~~1 °~~.5 °. We ~~see~~find a similar trend in relation to $\log_{10}$-binned surface roughness, with capture rates decreasing with increasing roughness, from ~90% (low roughness) to ~~10-20~~30-40% (once roughness ~~exceeds ~ 5~~reaches ~10 m). In both cases, we observe a difference of ~10-20% between the maximum possible percentage of topography that could be captured and the actual percentage captured~~. These discrepancies are slightly larger within~~ by the ~~range of rapid capture decline for both slope (~0.1-1 °) and roughness (~0.01-10 m).~~current BC-005 processing configuration.

Next, we assessed the mean proportion of the illuminated surface that was above, within, and below the range window. This allowed us to determine the degree to which the window was centered on the target surface, and how this varies as a function of slope and roughness (Figs. ~~4~~5 e and f). This analysis indicates that the ~10% of the illuminated topography not captured within the range window at lower values of slope and roughness ~~fall~~falls predominantly ~~above~~below the range window. As slope and roughness increases, topographic capture decreases, ~~due to~~with the proportion of topography above and below the range window increasing in approximately equal measures. Once slope and roughness exceed ~~1.3~~2 ° and ~~3~~7 m respectively, the proportion of topography below the range window begins to decrease, and is replaced with surface topography above the range window.

~~Finally, we~~In addition to assessing the dependency on surface slope and roughness, we also evaluated whether the heading of the satellite as it crosses the Antarctic coast ~~has~~had a significant impact on window placement. We found that 50.5% of records within 30 km of the coast were acquired in a configuration where the satellite was flying from land to ocean, and 49.5% from ocean to land. When the satellite is heading from land to ocean, we obtain a median topographic capture (with respect to the theoretical maximum) of ~~82.7~~87.0% for records within 30 km of the coast. Conversely, when the satellite flies from ocean to land, we obtain a median topographic capture of ~~83.5~~87.4%. With a difference of less than ~~1~~0.5%, we conclude that there is therefore insufficient evidence to suggest that coastal heading has a significant impact on the adequacy of window placement.

Within the preceding analysis, we have evaluated the extent to which the 60 m range window of Sentinel-3 impacts upon the instrument's capacity to capture the full topographic surface illuminated by the beam footprint. To conclude this component of our analysis, we therefore broadened the scope to consider how the statistics relating to the theoretically possible topographic capture were affected by varying sized range windows (Fig. 6). For a 60 m range window, the mean percentage of topography captured with optimal placement is 90.6%, with a standard deviation of 15.9%. As the range window increases, the mean topographic capture rises to 96.9% (120 m window), 98.4% (180 m), 99.0% (240 m), and 99.5% (360 m), with corresponding standard deviations of 10.5%, 7.7%, 6.0%, and 4.0%, respectively. The most substantial improvement occurs between 60 m and 120 m, with diminishing returns observed at larger window sizes. These findings also support the range window size chosen for the upcoming CRISTAL mission, which will

operate with a 256 m range window and interferometric (i.e. swath processing) capability over land ice (Kern et al., 2020).

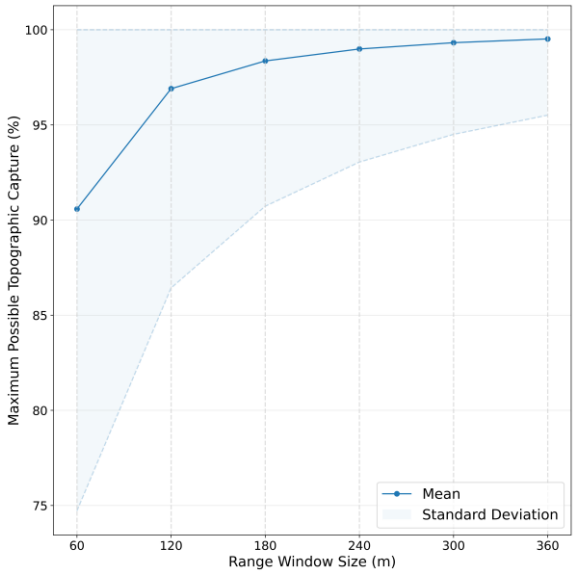

Maximum possible percentage of topography captured with optimal placement of the range window as a function of range window size. The shading shows the variability across records in the percentage of topographic capture, characterised by the standard deviations and limited at its maximum to 100%.

Capture of the Point of Closest Approach

~~Next, we analysed the effectiveness of the positioning of the Sentinel-3 L1b range window in capturing the POCA on the ice surface.~~Next, we analysed the positioning of the POCA identified in the Level-2 product, relative to the range window and beam-limited footprint, and compared this to the positioning of the geometric point of closest approach, as determined by minimising the distance between the satellite and the REMA surface. In practice, this was done by classifying every measurement according to its positioning relative to the range window (Fig. 7 a). In order to explore how performance varied spatially, we binned the L2 POCA classes (LPCs), and the ~~Roemer~~REMA-derived POCA classes (RPCs) to 5 km~~, taking~~ (Figs. 7 b and 8 b). As these data are discrete, the modal values were taken, so as to provide the most common class within each grid cell ~~(Figs. 5 B and 6 b).~~. Using our new slope and roughness derivations (Fig. 2), we also explored the relationships between these window placement classes and the topographic parameters~~.~~ (Fig. 7 and Fig. 8).

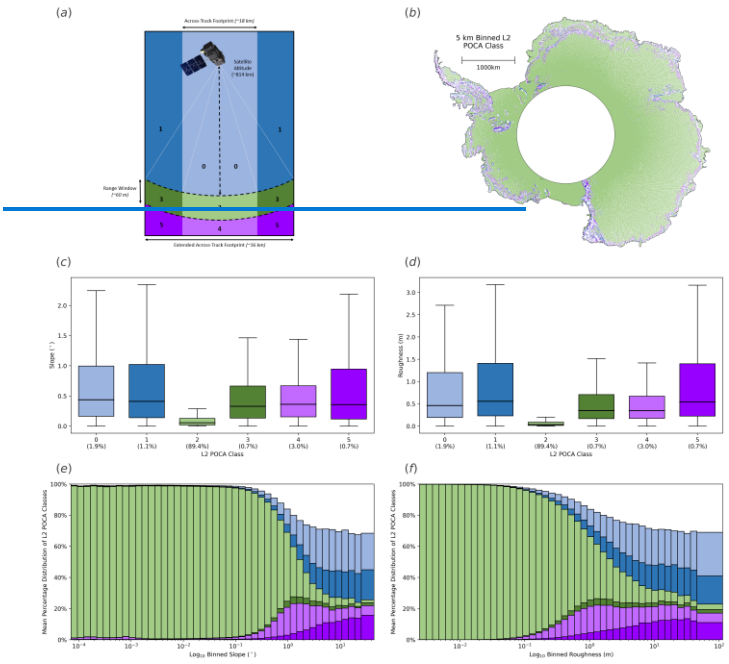
(a)
Across-Track Footprint (~10 km)
Satellite Altitude (~814 km)
Range Window (~60 m)
Extended Across-Track Footprint (~36 km)
(b)
5 km Binned L2 POCA Class
1000km
(c)
Slope (°)
L2 POCA Class
(d)
Roughness (m)
L2 POCA Class
(e)
Mean Percentage Distribution of L2 POCA Classes
Log10 Binned Slope (°)
(f)
Mean Percentage Distribution of L2 POCA Classes
Log10 Binned Roughness (m)

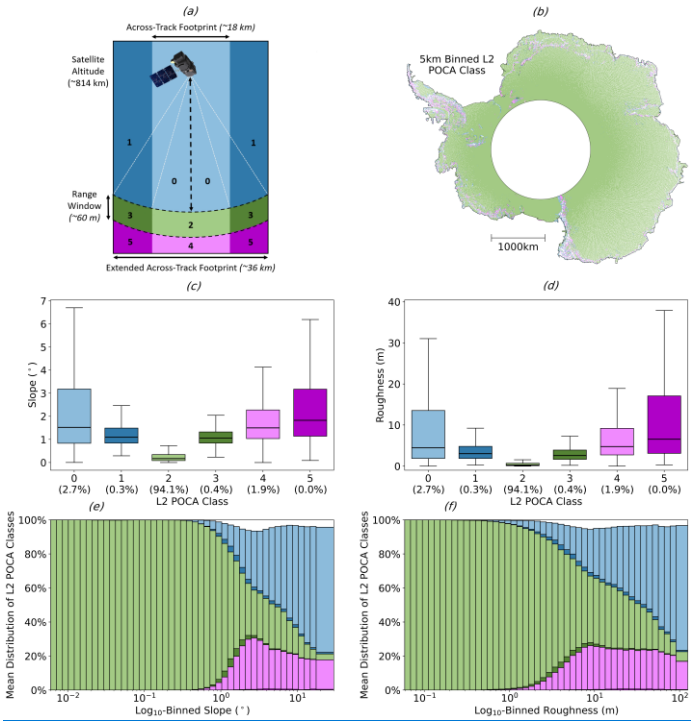

Assessment of the ability of Sentinel-3 to capture the surface reflection at the L2-derived POCA. Panel a outlines the POCA class definitions as per Fig. 1 for ease of cross-referencing. Panel b shows the L2-derived POCA classes, spatially binned to 5 km. Panels c and d show box plots of the L2-derived POCA per-class distribution with respect to slope and roughness, with the percentage of data within each class given in parentheses. Panels e and f show stacked bar charts representing the percentage distribution of the L2-derived POCA classes within each slope and roughness bin.

As a result of quality control and filtering in the L2 processing, we observe that ~~~3.19~~0.447% of the data is missing for the LPCs~~.~~ within the BC-005 product. This represents a significant improvement compared to the previous BC-004 product, wherein ~3.20% of the data were missing, primarily over topographically complex areas. The proportion of ~~this~~ missing data increases with slope and roughness, comprising ~~upwards of ~30~~5-10% of samples in regions of very high slope and roughness (Figs. ~~5~~7 e and f, respectively). For ~~89.4~~94.1% of the full, non-aggregated data, we observe that the L2 POCA lies within both the Sentinel-3 beam-limited footprint and the ~~L1b~~ range window. This occurs almost exclusively ~~at values~~in regions of ~~low~~lower slope and roughness, with a median of 0.~~0553 °~~170 ° and 0.~~0355~~277 m, and median absolute deviation of 0.~~0428 °~~105 ° and 0.~~0243~~189 m respectively (Figs. ~~5~~7 c and d). In contrast, the ~~other classes~~remaining

5.9% of acquisitions where the L2 POCA fails to be located within the range window encompass a far greater range of slope and roughness values, retaining significantly higher medians. This is evident spatially, with LPCs with a value other than 2 grouped around areas of complex topography such as the Transantarctic mountains, the Antarctic Peninsula, and coastal regions (Fig. 57 b). Comparing to the performance of the BC-004 product, again we find that the evolutions in BC-005 offer an improved capacity to derive a POCA that is consistent with the range window. Specifically, we find that BC-004 returned a lower (89.5%) percentage of records where the L2 POCA was correctly located within the range window and beam footprint (i.e. LPC class 2). Thus, the switch from BC-004 to BC-005 has approximately halved the proportion of acquisitions where the prescribed POCA location and the range window position are inconsistent.

We find that the proportion of L2 ~~POCA~~POCA's falling within both the beam-limited footprint and the range window (class 2) decreases with increasing slope and roughness. For both covariates~~,~~ (Figs. 7 e and f), the relationship follows ~~an approximate reverse-sigmoidal trend (Figs. 5 e and f), much like the~~ trends ~~found~~similar to those reported for topographic capture in Sect. 5.2. ~~This suggests~~We find that for ~~slope~~surface slopes (roughness) ~~values of~~ up to ~0.~~1 °~~ (3 ° (~ 0.3 m), the current window placement achieves near to 100% capture of the POCA location. As slope increases beyond this limit, however, ~~performance degrades~~the proportion of class 2 decreases, such that by ~1 °~~°~~ only ~~45~~70% of the L2 POCA's lie within the desired range, and by ~5 ° this reduces further to ~~5-10~~30% (Figs. 57 e and f). Likewise for roughness, we observe ~~an incremental~~a reduction in ~~performance up until~~the proportion of class 2 with increasing roughness, wherein by ~10 m~~, at which point~~ the proportion of ~~points falling within~~LPCs of class 2 ~~stabilises at ~5-10%~~reduces to ~40%, and further to ~20% by ~50 m (Figs. 57 e and f). With increasing slope and roughness, the observed reductions in class 2 are replaced in approximately equal parts by ~~the other classes, with slightly more cases of classes 0 and 1 (POCA above the range window) than 4 and 5 (POCA below the range window). While classes 0 and 1 increase at similar proportions, class 4 initially outweighs class 5, before class 5 begins to gradually dominate at extreme values of slope and roughness~~classes 0 (POCA above the range window) and 4 (POCA below the range window), up until ~3 ° slope and ~1 m roughness, wherein the increase in proportion of class 4 plateaus, and classes 0 dominate towards the extremes. This likely reflects the inability of the linear slope correction to adequately identify a point within the range window, in regions of high topographic variability. Notably, the occurrences of classes 1, 3, and 5, which constitute POCA locations outside of the beam-limited footprint, are negligible (0.3%, 0.4%, and 0.0%, respectively), and much lower than found in BC-004 (1.1%, 0.7%, and 0.7% respectively), likely a result of the algorithmic decision to avoid relocations beyond the 3 dB beamwidth.

The RPCs, which are defined using the location that minimises the range between the surface and satellite, rather than the location written in the Level-2 product, follow broadly the same distribution as the LPCs, with the exception of minimal data loss ~~(~~(~0.~~003~~00261%), which is simply due to missing data within the REMA dataset (Fig. ~~6~~8 b). ~~Similarly to the LPC's, 89.0~~Overall, 90.6% of the full, non-aggregated data has an RPC

of 2 (corresponding to a POCA within both the beam-limited footprint and range window), with median slope and roughness for this class of 0.0553163 ° and 0.0353259 m, respectfullyrespectively (Figs. 68 c and d). c and d). Notably, the BC-004 product classifies a slightly reduced 89.0% of class 2 RPCs, indicating improvements in the BC-005 product in its ability to capture the 'true' POCA (as defined by REMA), due to the extended window processing. The level of agreement on an RPC classification of 2 between the two product versions varies significantly with surface slope. For slopes of 0.0-1.0 °, 1.0-2.5 °, and ≥2.5 °, the percentage of records for which BC-004 and BC-005 agree is 93.6%, 19.0%, and 3.25%, respectively, illustrating the impact that the refined BC-005 processing is having for retrievals in topographically complex areas. In these same slope bins, the percentage of acquisitions where BC-005 correctly returns a class 2 classification, whereas BC-004 does not, is 1.93%, 13.8%, and 1.88%; whereas the converse case where BC-004 returns class 2 and BC-005 does not, occurs for only 0.766%, 3.04%, and 0.832% of records. A similar pattern is observed with respect to surface roughness. For roughness ranges of 0.0-5.0 m, 5.0-10 m, and ≥10 m, the percentage of records where BC-005 returns class 2 and BC-004 does not is 2.45%, 8.26%, and 2.10%, whereas the converse occurs for only 0.845%, 2.59%, and 1.23% of acquisitions. Together, these observations illustrate the improvements delivered by the latest baseline, and suggests that the extended window processing implemented in BC-005 is able to more reliably track the POCA in regions with more complex topographic terrain. Nonetheless, the fact that 64.1% and 94.0% of acquisitions in regions of 1.0-2.5 ° and ≥2.5 ° slope, respectively, do not have a REMA-derived POCA within the range window for either BC-004 or BC-005 illustrates the challenges presented by the relatively small 60 m range window in areas of complex topography, and the opportunity for further algorithmic evolution.

In comparison to the LPC's, the RPCs return more cases where the POCA is located above the range window, and less instances where the POCA is below the range window (Figs. 68 c and d). This is unsurprising given that the RPC approach, by minimising the range, favours the highest point within the footprint, which is more often above rather than below the range window. The With respect to slope and roughness, the RPC's exhibit very similar reverse-sigmoidal trends in class 2 as the LPC's, with thealthough there are a greater proportion of measurements that are located outside of the 3 dB beamwidth (1, 3, and 5), likely due to the fact that when we determine the RPC, we do not place any restrictions on it being within the 3 dB beamwidth. This highlights the fact that in areas of complex topography the point of closest approach can often be beyond the 3 dB beamwidth. The proportion of classes 0 and 1 also increasingincreases with slope and roughness in approximateapproximately equal parts. However, however, unlike the LPC's, classes 4 and 5 (POCA below the range window) experience only a temporary increase with increasing slope and roughness, peaking in the range ~1-10 meters and degrees, respectfullyat ~3 ° and ~9 m, respectively, before being replaced by classes 0 and 1 (POCA above the range window) for more extreme topographic variance (Figs. 68 e and f). We also foundfind that classes 4 and 5 often occur at the transition between floating and grounded ice (Fig. 68 b), where there is a rapid change in the surface gradient, and hence may be due to the inertia in the closed-loop tracker, which positions the range window based upon preceding

tracker information. As slope and roughness increase further, then classes 0 and 1 again dominate, reflecting the behaviour typical of mountainous terrain where local topographic highs exceed the positioning of the range window.

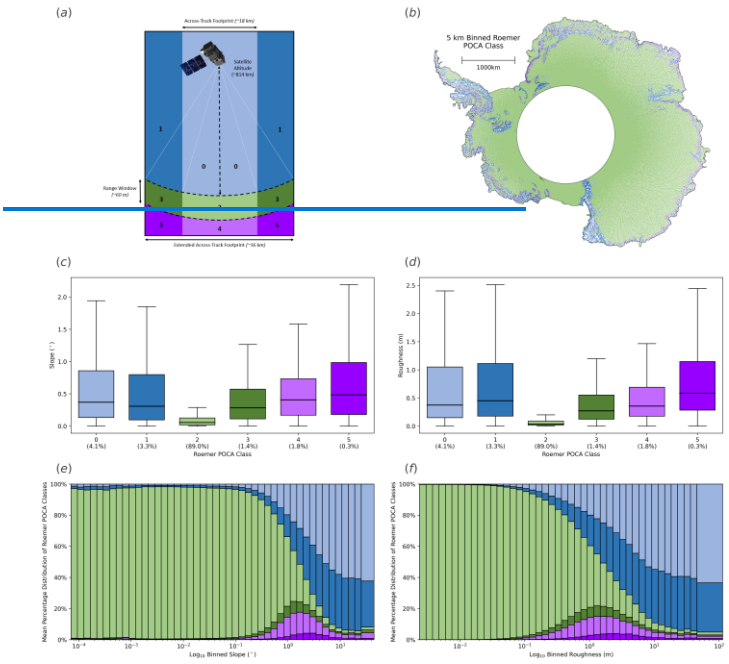
(a)
Across-Track Footprint (~10 km)
Satellite Altitude (~814 km)
Range Window (~60 m)
Extended Across-Track Footprint (~36 km)
(b)
5 km Binned Roemer POCA Class
1000km
(c)
Slope (°)
Roemer POCA Class
(d)
Roughness (m)
Roemer POCA Class
(e)
Mean Percentage Distribution of Roemer POCA Classes
Log10 Binned Slope (°)
(f)
Mean Percentage Distribution of Roemer POCA Classes
Log10 Binned Roughness (m)

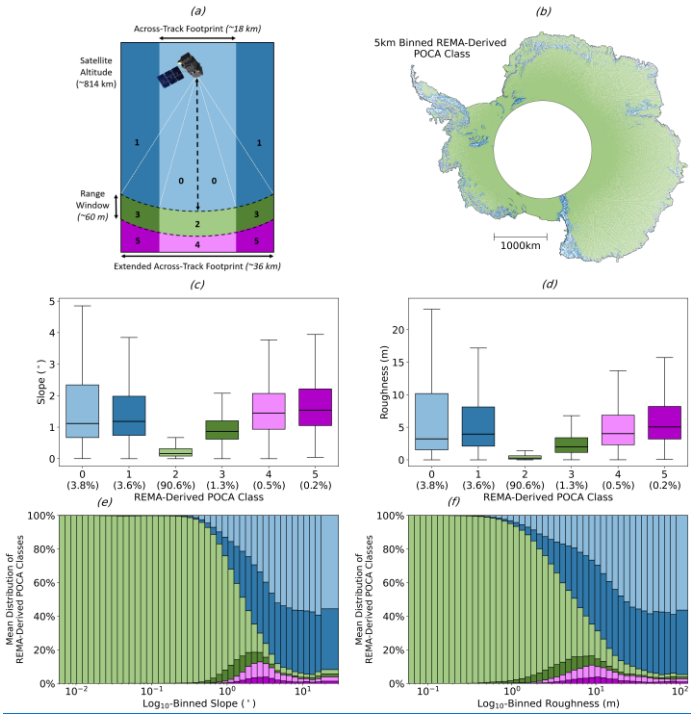

Assessment of the ability of Sentinel-3 to capture the surface reflection at the ~~Roemer~~REMA-derived POCA. Panel a outlines the POCA class definitions as per Fig. 1 for ease of cross-referencing. Panel b shows the ~~Roemer~~REMA-derived POCA classes, spatially binned to 5 km. Panels c and d show box plots of the ~~Roemer~~REMA-derived POCA classes with respect to slope and roughness. Panels e and f show stacked bar charts representing the percentage distribution of the ~~Roemer~~REMA-derived POCA classes with respect to log_{10}-binned slope and roughness.

Lastly, we again assessed whether the per-class distribution ~~close to the ice sheet coast~~ was affected by the satellite heading for ~~records~~acquisitions made within close proximity (within 30 km) of the ice sheet coast. For the RPCs, we observed that the range window was adequately placed (i.e. class 2) for ~~44.9~~50.4% of the measurements that were acquired when heading from land to ocean, and ~~45.4~~51.6% when heading from ocean to land. A difference of only ~~0.5~~1.2% suggests that ~~again~~ there is ~~insufficient~~no definitive evidence that coastal heading affects the per-class distribution close to the ice sheet coast, ~~agreeing with~~similar to the negligible difference in topographic capture rate (with respect to the theoretical maximum) that was observed ~~with respect to coastal heading (~~in Sect. 5.2~~).~~.

Along-track Correlation of Echoes

Our final set of analyses focuses on exploiting our new slope and roughness datasets to assess the correlation of series of altimetry echoes acquired along the orbit track, with a view to investigating the impact of surface topography on the degree of waveform correlation achieved. To investigate correlation across the entire ice sheet, we bin both the correlation between consecutive waveforms, and the fitted 50-record correlation change, taking the mean values within each 5x5 km grid cell (Figs. ~~7~~9 a and b). For the inter-record correlation, we found a median of 0.~~945~~944 and a median absolute deviation of 0.~~0284~~00300, with the distribution skewed towards higher correlation values, and lower values grouped around areas of topographic complexity (Fig. ~~7~~9 a). For the fitted 50-record correlation change, we found a median reduction in the correlation of -0.~~419~~418 over 15 km and a median absolute deviation of 0.~~0258. 4.71~~0250. 12.6% of records had a correlation change of less than -1 and were removed from our analysis (as discussed in Sect. 4.4). By comparing qualitatively to our REMA-derived estimates of across-track surface slope and roughness (Fig. 2), it is clear that both of these topographic parameters influence the degree of correlation between waveforms. For example, correlation reduces in areas of high roughness, such as megadune fields in East Antarctica, and high surface slope, such as the coastal margin of the ice sheet (Figs. ~~7~~9 a and b).

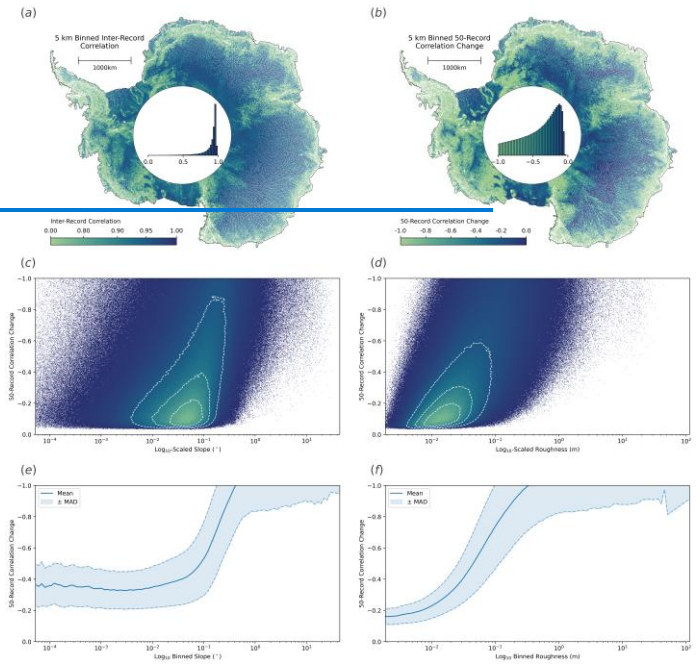
(a)
5 km Binned Inter-Record Correlation
1000km
Inter-Record Correlation
0.80
0.90
0.95
1.00
(b)
5 km Binned 50-Record Correlation Change
1000km
50-Record Correlation Change
−1.0
−0.8
−0.6
−0.4
−0.2
0.0
(c)
50-Record Correlation Change
Log10 Scaled Slope (°)
(d)
50-Record Correlation Change
Log10 Scaled Roughness (m)
(e)
Mean
± MAD
50-Record Correlation Change
Log10 Binned Slope (°)
(f)
Mean
± MAD
50-Record Correlation Change
Log10 Binned Roughness (m)

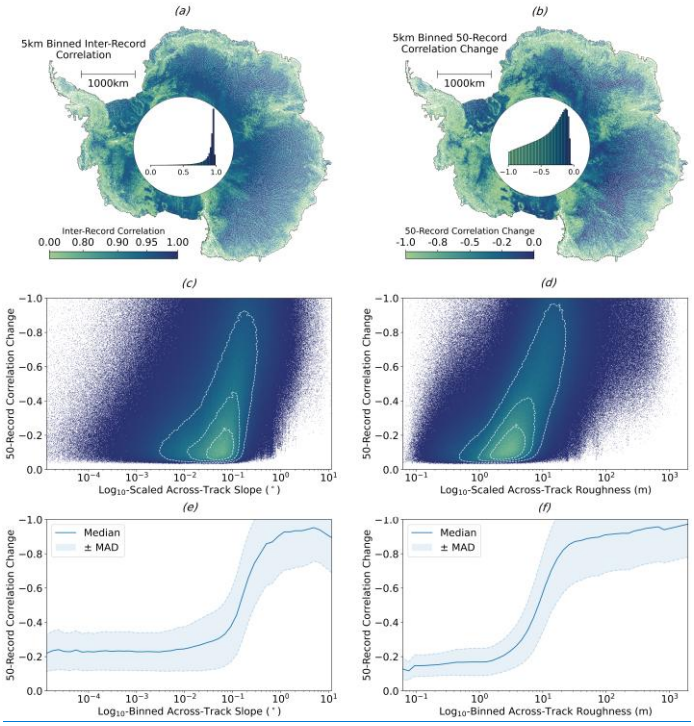

Analysis of the along-track correlation of Sentinel-3 SAR altimetry echoes. Panel a shows the correlation between consecutive records, spatially binned to 5 km. Panel b shows the 50-record correlation change, also spatially binned to 5 km. Histograms showing the overall distribution of each parameter are given within the pole holes of the respective plots. Panel c and d show density plots of the 50-record correlation change as a function of log_{10}-binned slope and roughness respectively. Concentric contours are included, which contain 75%, 50%, and 25% of the data from outside to in respectively. Panels e and f show the ~~mean~~median and median absolute deviation of the 50-record correlation change with respect to log_{10}-binned slope and roughness, respectively.

Comparing the fitted 50-record correlation change to across-track surface slope and roughness, we see that the 15 km change in correlation remains relatively stable at ~-0.~~35~~25, for slopes up to ~0.01~~,~~ °, before dropping rapidly to ~~-1~~~-0.95 for slopes above this value (Fig. ~~2~~9 e). For low surface roughness, the 50-record correlation change is ~-0.15, but this quickly drops ~~to -~~towards ~-1 once roughness exceeds ~~~0.~~~2 m (Fig. ~~2~~9 f). Taking the Pearson correlation coefficient of the 50-record correlation change to log_{10}-binned surface slope and roughness we find values of -0.~~534 (p-value < 0.01)~~618 and -0.~~342 (p-value of 0.0199).~~571. This implies that, linearly, slope and roughness explain ~~28.5~~38.2%

and ~~11.7~~22.2% of the ice-sheet wide variance in along-track waveform decorrelation. We therefore conclude that~~, at the 5% significance level,~~ 50-record correlation change is moderately, linearly correlated to $\log_{10}$-binned surface slope and $\log_{10}$-binned roughness, with slope providing a stronger control. Whilst conceptually, it is understood that slope and roughness impact the shape of the echo, and associated parameters such as the number of peaks, leading edge width, and trailing edge slope, this analysis demonstrates quantitatively the strength of this correlation, through the comparison of independent altimetry and DEM-derived datasets.

Conclusions

Since the launch of Sentinel-3A in 2016, and Sentinel-3B in 2018, the Sentinel-3 mission has acquired hundreds of millions of echoes over Antarctica, providing topographic information at ~~resolutions~~a resolution of ~300 m along-track by ~1.6-2 km across-track, which are repeated every ~27 days. To date, however, previous assessments of Sentinel-3 performance over ice sheets have concentrated predominantly on the outputs of L2 processors, namely the high-level validation of the resulting elevation products. Here, we extend previous work by using novel topographic datasets derived from REMA, to more directly explore the underlying factors that influence Sentinel-3's performance. Specifically, we use ~~singular value decomposition~~Singular Value Decomposition to robustly separate local elevation variability into slope and roughness components, and investigate the impact of each upon Sentinel-3 altimeter performance.

Quantitatively, our new estimates of slope and roughness indicate a strong positive correlation (Pearson correlation coefficient of 0.~~730~~808) between these two variables; areas with higher surface slopes also exhibit greater kilometre-scale (orthogonal) surface roughness. Overall, we find that ~~57.4~~76.9% and ~~90~~89.1% of the ice sheet ~~exhibited~~exhibits slopes below 0.~~1~~5 and 1.0~~.5°~~, °, respectively; and ~~64.9~~62.4% and ~~89.5% had~~76.1% has a roughness lower than 0.~~1~~5 and 1.0~~.5~~ m, respectively (where roughness is defined as the ~~standard deviation~~minimum-to-maximum difference of the orthogonal residuals). Qualitatively, our new slope and roughness maps display a wealth of glaciological information, including ice shelf flow patterns and the locations of megadune fields in East Antarctica. These findings enhance our understanding of the AIS's geometrical properties and represent, to the best of our knowledge, the first continent-wide analysis of Antarctic surface roughness, that is independent of slope.

During operation, the Sentinel-3 onboard tracker aims to position the ~~L1b~~ range window so that it captures the underlying topographic surface. One way to measure its ~~successes~~success in doing so, whilst acknowledging the inherent limitations imposed by the range window dimension, is to assess the proportion of the surface illuminated by the instrument that falls within the range window. Performing such an assessment at the ice sheet scale, through the analysis of over 8 million echoes, we find that in ~~23.7~~57.4% of cases, capturing the full topography within the beam-limited footprint is impossible, due to the relatively small ~60 m ~~L1b~~ range window of Sentinel-3, relative to the high topographic variance found across some regions of the ice sheet. Nonetheless, our analysis shows that

with optimal placement of the range window, 80% of the illuminated topographic surface could be captured in ~80% of cases. Building on this, we ~~also~~ investigated the performance of the current window placement, by measuring the ratio of actual topographic capture to the maximum possible capture that could be achieved with an adjusted ~~position~~placement of the range window. On average, the current placement achieved a median of 89.~~7 ± 3.27~~2 ± 2.46% of total possible topographic capture, with this value decreasing with increasing slope and roughness. ~~This~~Broader analysis of the relationship between the range window size and the maximum achievable topographic capture showed that substantial gains can ~~inform further refinement~~be achieved by increasing the range window beyond 60 m. Doubling the window size to 120 m, for example, could increase the mean capture from 90.6% to 96.9%. Together, this analysis serves to provide a better understanding of the performance of the Sentinel-3 onboard tracker, on-ground processing, and also ~~serve~~ to support the design of future missions, by providing empirical information with which to optimise the size and positioning of the range window.

Within ~~the~~current Level-2 ~~Sentinel-3 altimetry product,~~ processing schemes, there is an implicit assumption ~~is made~~ that the ~~echoing~~prescribed point ~~(the so-called~~ of closest approach (POCA) lies within ~~the intersection of the range window and the~~ both the instrument's beam-limited footprint~~.~~ and its range window, and hence that the range to the waveform leading edge corresponds to the distance between the satellite and the identified POCA. To ~~investigate~~evaluate this assumption, we ~~classified~~compared the ~~location~~locations of the ~~specified L2 POCA, along with our own POCA that was derived by minimising the range to the illuminated REMA surface, relative~~L2-designated POCA in two product versions (BC-004 and BC-005) to the position of ~~the Sentinel-3 L1b~~ range window~~. We found that the assumption that~~ for ~8 million acquisitions collected over the Antarctic Ice Sheet, in addition to that of an independent POCA estimate that we derived from a high resolution DEM. This analysis showed that the current window placement successfully captures the point of closest approach for 90.6% of acquisitions and allowed us to investigate, quantitatively, the ~~L2 POCA falls within~~ improvements offered by the ~~range window was correct for 89.4% of the data, with failures becoming more common with increasing slope and roughness. Our Roemer-derived echoing points exhibited similar patterns to that of the L2, with POCA being captured by the range~~BC-005 extended window ~~in 89.0% of cases. From this analysis, it is clear that for ~10%~~processing, in areas of ~~the ice sheet, in regions of more~~ complex ~~topography, the algorithms used to relocate the echo can be improved~~topographic terrain.

Finally, we explored the correlation between sequences of altimetry echoes along the satellite orbit track, to provide a first assessment of how surface topography affects waveform decorrelation. We found that inter-record correlation was generally high, but decreased in areas with complex topography. Similarly, taking the larger-scale correlation change across 50-records (spanning ~15 km) indicated that the rate of decorrelation was more rapid in regions with high surface slope and roughness. This analysis therefore provides direct evidence of the relationship between surface topography and along-track

altimetry echo correlation at the ice sheet scale, ~~thereby enhancing our understanding of~~offering new insight into how surface morphology influences waveform structure.

More broadly, this ~~dependency. This~~ study has shown how a new generation of high-resolution DEMs can be used to assess and understand the performance of current altimetry in-flight systems and on-the-ground processing. This information provides new insight to help understand the current performance of the Sentinel-3 fleet of satellite altimeters, and also serves as a template for future analysis that can guide the design and optimisation of planned missions such as the Copernicus Polar Ice and Snow Topography Altimeter (CRISTAL~~).~~) and the Sentinel-3 Next Generation Topography mission.

Abdalla, S., Abdeh Kolahchi, A., Ablain, M., Adusumilli, S., Aich Bhowmick, S., Alou-Font, E., Amarouche, L., Andersen, O. B., Antich, H., Aouf, L., Arbic, B., Armitage, T., Arnault, S., Artana, C., Aulicino, G., Ayoub, N., Badulin, S., Baker, S., Banks, C., … Zlotnicki, V. (2021). Altimetry for the future: Building on 25 years of progress. *Advances in Space Research*, *68*(2), 319–363. https://doi.org/https://doi.org/10.1016/j.asr.2021.01.022

and, J. L. B. (1994). Ice sheet altimeter processing scheme. *International Journal of Remote Sensing*, *15*(4), 925–938. https://doi.org/10.1080/01431169408954125

Aublanc, J., Boy, F., Borde, F., & Féménias, P. (2024). A facet based numerical model to retrieve ice sheet topography from sentinel-3 altimetry. *EGUsphere*, *2024*, 1–26. https://doi.org/10.5194/egusphere-2024-1323

Aublanc, J., Féménias, P., Catapano, F., & Chamayou, A. (2024). *Sentinel-3 SRAL/MWR land user handbook* (Technical Report S3MPC-STM_RP_0038). S3 Mission Performance Centre (S3MPC). https://sentiwiki.copernicus.eu/__attachments/1672112/S3MPC-STM_RP_0038%20-%20Sentinel-3%20SRAL%20Land%20User%20Handbook%202024%20-%201.2.pdf?inst-v=42421289-0f0f-482d-98b0-4ef0b5af900d

Aublanc, J., Moreau, T., Thibaut, P., Boy, F., Rémy, F., & Picot, N. (2018). Evaluation of SAR altimetry over the antarctic ice sheet from CryoSat-2 acquisitions. *Advances in Space Research*, *62*(6), 1307–1323. https://doi.org/https://doi.org/10.1016/j.asr.2018.06.043

Aublanc, J., Renou, J., Piras, F., Nielsen, K., Rose, S. K., Simonsen, S. B., Fleury, S., Hendricks, S., Taburet, N., D'Apice, G., Chamayou, A., Féménias, P., Catapano, F., & Restano, M. (2025). Sentinel-3 altimetry thematic products for hydrology, sea ice and land ice. *Scientific Data*, *12*(1), 714. https://doi.org/10.1038/s41597-025-04956-3

Birkett, C. M., & Beckley, B. (2010). Investigating the performance of the jason-2/OSTM radar altimeter over lakes and reservoirs. *Marine Geodesy*, *33*(sup1), 204–238. https://doi.org/10.1080/01490419.2010.488983

Blarel, F., Frappart, F., Legrésy, B., Blumstein, D., Rémy, F., Fatras, C., Mougin, E., Papa, F., Prigent, C., Niño, F., et al. (2015). Altimetry backscattering signatures at ku and s bands

over land and ice sheets. *Remote Sensing for Agriculture, Ecosystems, and Hydrology XVII*, *9637*, 315–324. https://doi.org/10.1117/12.2194498

Brenner, A. C., Blndschadler, R. A., Thomas, R. H., & Zwally, H. J. (1983). Slope-induced errors in radar altimetry over continental ice sheets. *Journal of Geophysical Research: Oceans*, *88*(C3), 1617–1623. https://doi.org/10.1029/JC088iC03p01617

Brenner, A. C., DiMarzio, J. P., & Zwally, H. J. (2007). Precision and accuracy of satellite radar and laser altimeter data over the continental ice sheets. *IEEE Transactions on Geoscience and Remote Sensing*, *45*(2), 321–331. https://doi.org/10.1109/TGRS.2006.887172

Brown, G. (1977). The average impulse response of a rough surface and its applications. *IEEE Transactions on Antennas and Propagation*, *25*(1), 67–74. https://doi.org/10.1109/TAP.1977.1141536

Chartrand, A. M., & Howat, I. M. (2020). Basal channel evolution on the getz ice shelf, west antarctica. *Journal of Geophysical Research: Earth Surface*, *125*(9), e2019JF005293. https://doi.org/10.1029/2019JF005293

Chuter, S. J., & Bamber, J. L. (2015). Antarctic ice shelf thickness from CryoSat-2 radar altimetry. *Geophysical Research Letters*, *42*(24), 10, 721–710, 729. https://doi.org/https://doi.org/10.1002/2015GL066515

Clerc, S., Donlon, C., Borde, F., Lamquin, N., Hunt, S. E., Smith, D., McMillan, M., Mittaz, J., Woolliams, E., Hammond, M., et al. (2020). Benefits and lessons learned from the sentinel-3 tandem phase. *Remote Sensing*, *12*(17), 2668. https://doi.org/10.3390/rs12172668

Clerc, S., Donlon, C., Borde, F., Lamquin, N., Hunt, S. E., Smith, D., McMillan, M., Mittaz, J., Woolliams, E., Hammond, M., Banks, C., Moreau, T., Picard, B., Raynal, M., Rieu, P., & Guérou, A. (2020). Benefits and lessons learned from the sentinel-3 tandem phase. *Remote Sensing*, *12*(17). https://doi.org/10.3390/rs12172668

Cooper, A. P. R. (1989). Slope correction by relocation for satellite radar altimetry. *12th Canadian Symposium on Remote Sensing Geoscience and Remote Sensing Symposium*, *4*, 2730–2733. https://doi.org/10.1109/IGARSS.1989.577978

Curlander, J. C., & McDonough, R. N. (1991). *Synthetic aperture radar* (Vol. 11). Wiley, New York.

Davis, C. H. (1997). A robust threshold retracking algorithm for measuring ice-sheet surface elevation change from satellite radar altimeters. *IEEE Transactions on Geoscience and Remote Sensing*, *35*(4), 974–979. https://doi.org/10.1109/36.602540

Davis, C. H., Li, Y., McConnell, J. R., Frey, M. M., & Hanna, E. (2005). Snowfall-driven growth in east antarctic ice sheet mitigates recent sea-level rise. *Science*, *308*(5730), 1898–1901. https://doi.org/10.1126/science.1110662

Dawson, G. J., & Bamber, J. L. (2017). Antarctic grounding line mapping from CryoSat-2 radar altimetry. *Geophysical Research Letters*, *44*(23), 11, 886–811, 893. https://doi.org/https://doi.org/10.1002/2017GL075589

Donlon, C., Berruti, B., Buongiorno, A., Ferreira, M.-H., Féménias, P., Frerick, J., Goryl, P., Klein, U., Laur, H., Mavrocordatos, C., et al. (2012). The global monitoring for environment and security (GMES) sentinel-3 mission. *Remote Sensing of Environment*, *120*, 37–57. https://doi.org/10.1016/j.rse.2011.07.024

Donlon, C., Berruti, B., Mecklenberg, S., Nieke, J., Rebhan, H., Klein, U., Buongiorno, A., Mavrocordatos, C., Frerick, J., Seitz, B., et al. (2012). The sentinel-3 mission: Overview and status. *2012 IEEE International Geoscience and Remote Sensing Symposium*, 1711–1714. https://doi.org/10.1109/IGARSS.2012.6351194

~~Ehlers, F., Schlembach, F., Kleinherenbrink, M., & Slobbe, C.~~ EUMETSAT. (2017). *Sentinel-3 SRAL marine user handbook*. EUMETSAT; Public document. http://www.eumetsat.int/website/home/Technical/Applications/index.html

~~(2023). Validity assessment of SAMOSA retracking for fully-focused SAR altimeter waveforms. *Advances in Space Research*, *71*(3), 1377–1396. https://doi.org/10.1016/j.asr.2022.11.034~~

Frederikse, T., Buchanan, M. K., Lambert, E., Kopp, R. E., Oppenheimer, M., Rasmussen, D., & Wal, R. S. van de. (2020). Antarctic ice sheet and emission scenario controls on 21st-century extreme sea-level changes. *Nature Communications*, *11*(1), 390. https://doi.org/10.1038/s41467-019-14049-6

Gourmelen, N., Goldberg, D. N., Snow, K., Henley, S. F., Bingham, R. G., Kimura, S., Hogg, A. E., Shepherd, A., Mouginot, J., Lenaerts, J. T. M., Ligtenberg, S. R. M., & Berg, W. J. van de. (2017). Channelized melting drives thinning under a rapidly melting antarctic ice shelf. *Geophysical Research Letters*, *44*(19), 9796–9804. https://doi.org/https://doi.org/10.1002/2017GL074929

Griggs, J. A., & Bamber, J. L. (2011). Antarctic ice-shelf thickness from satellite radar altimetry. *Journal of Glaciology*, *57*(203), 485–498. https://doi.org/10.3189/002214311796905659

Helm, V., Humbert, A., & Miller, H. (2014). Elevation and elevation change of greenland and antarctica derived from CryoSat-2. *The Cryosphere*, *8*(4), 1539–1559. https://doi.org/10.5194/tc-8-1539-2014

Hogg, A. E., Shepherd, A., Gilbert, L., Muir, A., & Drinkwater, M. R. (2018). Mapping ice sheet grounding lines with CryoSat-2. *Advances in Space Research*, *62*(6), 1191–1202. https://doi.org/https://doi.org/10.1016/j.asr.2017.03.008

Horn, B. K. P., & Schunck, B. G. (1981). Determining optical flow. *Artificial Intelligence*, *17*(1), 185–203. https://doi.org/10.1016/0004-3702(81)90024-2

Howat, I. M., Porter, C., Smith, B. E., Noh, M.-J., & Morin, P. (2019). The reference elevation model of antarctica. *The Cryosphere*, *13*(2), 665–674. https://doi.org/10.5194/tc-13-665-2019

Howat, I., Morin, P., Porter, C., & Noh, M.-J. (2018). *The Reference Elevation Model of Antarctica, Version 1* (Version V1). Harvard Dataverse. https://doi.org/10.7910/DVN/SAIK8B

Huang, Q., McMillan, M., Muir, A., Phillips, J., & Slater, T. (2024). Multipeak retracking of radar altimetry waveforms over ice sheets. *Remote Sensing of Environment*, *303*, 114020. https://doi.org/https://doi.org/10.1016/j.rse.2024.114020

IPF. (2024). *Sentinel-3 level 2 SRAL SM2 - LI algorithm theoretical baseline definition* (S3MPC.ATBD.LI, Issue 4.3). Sentinel-3 Mission Performance Centre (S3MPC).

Kern, M., Cullen, R., Berruti, B., Bouffard, J., Casal, T., Drinkwater, M. R., Gabriele, A., Lecuyot, A., Ludwig, M., Midthassel, R., Navas Traver, I., Parrinello, T., Ressler, G., Andersson, E., Martin-Puig, C., Andersen, O., Bartsch, A., Farrell, S., Fleury, S., … Yackel, J. (2020). The copernicus polar ice and snow topography altimeter (CRISTAL) high-priority candidate mission. *The Cryosphere*, *14*(7), 2235–2251. https://doi.org/10.5194/tc-14-2235-2020

Konrad, H., Shepherd, A., Gilbert, L., Hogg, A. E., McMillan, M., Muir, A., & Slater, T. (2018). Net retreat of antarctic glacier grounding lines. *Nat. Geosci.*, *11*(4), 258–262.

Kovaly, J. J. (1976). Synthetic aperture radar. *Dedham*.

Landy, J. C., Tsamados, M., & Scharien, R. K. (2019). A facet-based numerical model for simulating SAR altimeter echoes from heterogeneous sea ice surfaces. *IEEE Transactions on Geoscience and Remote Sensing*, *57*(7), 4164–4180. https://doi.org/10.1109/TGRS.2018.2889763

Legresy, B., Papa, F., Remy, F., Vinay, G., van den Bosch, M., & Zanife, O.-Z. (2005). ENVISAT radar altimeter measurements over continental surfaces and ice caps using the ICE-2 retracking algorithm. *Remote Sensing of Environment*, *95*(2), 150–163. https://doi.org/https://doi.org/10.1016/j.rse.2004.11.018

Levinsen, J. F., Simonsen, S. B., Sørensen, L. S., & Forsberg, R. (2016a). The impact of DEM resolution on relocating radar altimetry data over ice sheets. *IEEE Journal of Selected Topics in Applied Earth Observations and Remote Sensing*, *9*(7), 3158–3163. https://doi.org/10.1109/JSTARS.2016.2587684

Levinsen, J. F., Simonsen, S. B., Sørensen, L. ~~2016~~S., & Forsberg, R. (2016b). The impact of DEM resolution on relocating radar altimetry data over ice sheets. *IEEE Journal of Selected Topics in Applied Earth Observations and Remote Sensing*, *9*(7), 3158–3163. https://doi.org/10.1109/JSTARS.2016.2587684

Li, W., Slobbe, C., & Lhermitte, S. (2022). A leading-edge-based method for correction of slope-induced errors in ice-sheet heights derived from radar altimetry. *The Cryosphere*, *16*(6), 2225–2243. https://doi.org/10.5194/tc-16-2225-2022

Liu, M., Wang, Z., Zhang, B., Wu, S., & An, J. (2023). Extraction and analysis of the antarctic ice shelf basal channel. *IEEE Geoscience and Remote Sensing Letters*, *20*, 1–5. https://doi.org/10.1109/LGRS.2023.3304350

Love, A. (1985). In memory of carl a. wiley. *IEEE Antennas and Propagation Society Newsletter*, *27*(3), 17–18. https://doi.org/10.1109/MAP.1985.27810

Martin, T. V., Zwally, H. J., Brenner, A. C., & Bindschadler, R. A. (1983). Analysis and retracking of continental ice sheet radar altimeter waveforms. *Journal of Geophysical Research: Oceans*, *88*(C3), 1608–1616. https://doi.org/10.1029/JC088iC03p01608

McMillan, M., Corr, H., Shepherd, A., Ridout, A., Laxon, S., & Cullen, R. (2013). Three-dimensional mapping by CryoSat-2 of subglacial lake volume changes. *Geophysical Research Letters*, *40*(16), 4321–4327. https://doi.org/https://doi.org/10.1002/grl.50689

McMillan, M., Muir, A., & Donlon, C. (2021). Brief communication: Ice sheet elevation measurements from the sentinel-3A and sentinel-3B tandem phase. *The Cryosphere*, *15*(7), 3129–3134. https://doi.org/10.5194/tc-15-3129-2021

McMillan, M., Muir, A., Shepherd, A., Escolà, R., Roca, M., Aublanc, J., Thibaut, P., Restano, M., Ambrozio, A., & Benveniste, J. (2019). Sentinel-3 delay-doppler altimetry over antarctica. *The Cryosphere*, *13*(2), 709–722. https://doi.org/10.5194/tc-13-709-2019

Mertikas, S., Tripolitsiotis, A., Donlon, C., Mavrocordatos, C., Féménias, P., Borde, F., Frantzis, X., Kokolakis, C., Guinle, T., Vergos, G., et al. (2020). The ESA permanent facility for altimetry calibration: Monitoring performance of radar altimeters for sentinel-3A, sentinel-3B and jason-3 using transponder and sea-surface calibrations with FRM standards. *Remote Sensing*, *12*(16), 2642. https://doi.org/10.3390/rs12162642

Otosaka, I. N., Shepherd, A., Ivins, E. R., Schlegel, N.-J., Amory, C., Broeke, M. R. van den, Horwath, M., Joughin, I., King, M. D., Krinner, G., Nowicki, S., Payne, A. J., Rignot, E., Scambos, T., Simon, K. M., Smith, B. E., Sørensen, L. S., Velicogna, I., Whitehouse, P. L., … Wouters, B. (2023). Mass balance of the greenland and antarctic ice sheets from 1992 to 2020. *Earth System Science Data*, *15*(4), 1597–1616. https://doi.org/10.5194/essd-15-1597-2023

Passaro, M., Rautiainen, L., Dettmering, D., Restano, M., Hart-Davis, M. G., Schlembach, F., Särkkä, J., Müller, F. L., Schwatke, C., & Benveniste, J. (2022). Validation of an empirical subwaveform retracking strategy for SAR altimetry. *Remote Sensing*, *14*(16). https://doi.org/10.3390/rs14164122

Price, S. F., Payne, A. J., Howat, I. M., & Smith, B. E. (2011). Committed sea-level rise for the next century from greenland ice sheet dynamics during the past decade. *Proceedings*

of the National Academy of Sciences, *108*(22), 8978–8983. https://doi.org/10.1073/pnas.1017313108

Pritchard, H. D., Luthcke, S. B., & Fleming, A. H. (2010). Understanding ice-sheet mass balance: Progress in satellite altimetry and gravimetry. *Journal of Glaciology*, *56*(200), 1151–1161. https://doi.org/10.3189/002214311796406194

Quartly, G. D., Nencioli, F., Raynal, M., Bonnefond, P., Nilo Garcia, P., Garcia-Mondéjar, A., Flores de la Cruz, A., Crétaux, J.-F., Taburet, N., Frery, M.-L., et al. (2020). The roles of the S3MPC: Monitoring, validation and evolution of sentinel-3 altimetry observations. *Remote Sensing*, *12*(11), 1763. https://doi.org/10.3390/rs12111763

Quartly, G. D., Nencioli, F., Raynal, M., Bonnefond, P., Nilo Garcia, P., Garcia-Mondéjar, A., Flores de la Cruz, A., Crétaux, J.-F., Taburet, N., Frery, M.-L., Cancet, M., Muir, A., Brockley, D., McMillan, M., Abdalla, S., Fleury, S., Cadier, E., Gao, Q., Escorihuela, M. J., … Lucas, B. (2020). The roles of the S3MPC: Monitoring, validation and evolution of sentinel-3 altimetry observations. *Remote Sensing*, *12*(11). https://doi.org/10.3390/rs12111763

Quartly, G. D., Rinne, E., Passaro, M., Andersen, O. B., Dinardo, S., Fleury, S., Guillot, A., Hendricks, S., Kurekin, A. A., Müller, F. L., Ricker, R., Skourup, H., & Tsamados, M. (2019). Retrieving sea level and freeboard in the arctic: A review of current radar altimetry methodologies and future perspectives. *Remote Sensing*, *11*(7). https://doi.org/10.3390/rs11070881

Raney, R. K. (1998). The delay/doppler radar altimeter. *IEEE Transactions on Geoscience and Remote Sensing*, *36*(5), 1578–1588. https://doi.org/10.1109/36.718861

Ray, C., Martin-Puig, C., Clarizia, M. P., Ruffini, G., Dinardo, S., Gommenginger, C., & Benveniste, J. (2015). SAR altimeter backscattered waveform model. *IEEE Transactions on Geoscience and Remote Sensing*, *53*(2), 911–919. https://doi.org/10.1109/TGRS.2014.2330423

Remy, F., Mazzega, P., Houry, S., Brossier, C., & Minster, J. F. (1989). Mapping of the topography of continental ice by inversion of satellite-altimeter data. *Journal of Glaciology*, *35*(119), 98–107. https://doi.org/10.3189/002214389793701419

Rignot, Rémy, F., & Parouty, S. (2009). Antarctic ice sheet and radar altimetry: A review. *Remote Sensing*, *1*(4), 1212–1239. https://doi.org/10.3390/rs1041212

Ridley, J. K., & Partington, K. C. (1988). A model of satellite radar altimeter return from ice sheets. *International Journal of Remote Sensing*, *9*(4), 601–624. https://doi.org/10.1080/01431168808954881

E., Mouginot, J., & Scheuchl, B. (2011). Antarctic grounding line mapping from differential satellite radar interferometry. *Geophysical Research Letters*, *38*(10). https://doi.org/https://doi.org/10.1029/2011GL047109

Rignot, E., Mouginot, J., Scheuchl, B., Van Den Broeke, M., Van Wessem, M. J., & Morlighem, M. (2019). Four decades of antarctic ice sheet mass balance from 1979–2017. *Proceedings of the National Academy of Sciences*, *116*(4), 1095–1103. https://doi.org/10.1073/pnas.1812883116

Riley, S., Degloria, S., & Elliot, S. D. (1999). A terrain ruggedness index that quantifies topographic heterogeneity. *Internation Journal of Science*, *5*, 23–27.

Roemer, S., Legrésy, B., Horwath, M., & Dietrich, R. (2007). Refined analysis of radar altimetry data applied to the region of the subglacial lake vostok/antarctica. *Remote Sensing of Environment*, *106*(3), 269–284. https://doi.org/10.1016/j.rse.2006.02.026

Rosen, P. A., Hensley, S., Joughin, I. R., Li, F. K., Madsen, S. N., Rodriguez, E., & Goldstein, R. M. (2000). Synthetic aperture radar interferometry. *Proceedings of the IEEE*, *88*(3), 333–382. https://doi.org/10.1109/5.838084

S3-MPC. (2022). Sentinel-3 SRAL land user handbook. In *Sentinel-3 SRAL Land User Handbook*. ESA. https://sentinels.copernicus.eu/documents/247904/4871083/Sentinel-3+SRAL+Land+User+Handbook+V1.1.pdf/ebd1444d-240f-70ab-f8fc-e84b67b022cd?t=1673614240693

Sappington, J. M., Longshore, K. M., & Thompson, D. B. (2007). Quantifying landscape ruggedness for animal habitat analysis: A case study using bighorn sheep in the mojave desert. *Journal of Wildlife Management*, *71*(5), 1419–1426. https://doi.org/10.2193/2005-723

SentiWiki. (n.d.). *S3 altimetry instruments*. https://sentiwiki.copernicus.eu/web/s3-altimetry-instruments

Shepherd, A., Gilbert, L., Muir, A. S., Konrad, H., McMillan, M., Slater, T., Briggs, K. H., Sundal, A. V., Hogg, A. E., & Engdahl, M. E. (2019). Trends in antarctic ice sheet elevation and mass. *Geophysical Research Letters*, *46*(14), 8174–8183. https://doi.org/10.1029/2019GL082182

Shepherd, A., Wingham, D., & Rignot, E. (2004). Warm ocean is eroding west antarctic ice sheet. *Geophysical Research Letters*, *31*(23). https://doi.org/10.1029/2004GL021106

Siegert, M. J., Ross, N., & Le Brocq, A. M. (2016). Recent advances in understanding antarctic subglacial lakes and hydrology. *Philosophical Transactions of the Royal Society A: Mathematical, Physical and Engineering Sciences*, *374*(2059), 20140306. https://doi.org/10.1098/rsta.2014.0306

Siegfried, M. R., & Fricker, H. A. (2018). Thirteen years of subglacial lake activity in antarctica from multi-mission satellite altimetry. *Annals of Glaciology*, *59*(76pt1), 42–55. https://doi.org/10.1017/aog.2017.36

Simonsen, S. B., Barletta, V. R., Colgan, W. T., &Slater, T., Shepherd, A., Mcmillan, M., Armitage, T. W. K., Otosaka, I., & Arthern, R. J. (2019). Compensating changes in the penetration depth of pulse-limited radar altimetry over the greenland ice sheet. *IEEE Transactions on Geoscience and Remote Sensing*, *57*(12), 9633–9642. https://doi.org/10.1109/TGRS.2019.2928232

Slater, T., Shepherd, A., McMillan, M., Leeson, A., Gilbert, L., Muir, A., Munneke, P. K., Noël, B., Fettweis, X., Broeke, M. van den, & Briggs, K. (2021). Increased variability in greenland ice sheet runoff from satellite observations. *Nat. Commun.*, *12*(1), 6069.

Smith, B. (2021). *ICESat-2 algorithm theoretical basis document (ATBD) for land-ice DEM (ATL14) and land-ice height change (ATL15)* (Release 001). National Aeronautics; Space Administration (NASA), Goddard Space Flight Center.

Smith, B., Jelley, B., Dickinson, S., Sutterley, T., Neumann, T., & Harbeck, K. (2021). *ATLAS/ICESat-2 L3B gridded antarctic and arctic land ice height, version 1*. NASA National Snow; Ice Data Center Distributed Active Archive Center. https://doi.org/10.5067/ATLAS/ATL14.001

Sørensen, L. S. (2021). Greenland ice sheet mass balance (1992–2020) from calibrated radar altimetry. *Geophysical Research Letters*, *48*(3), e2020GL091216. https://doi.org/https://doi.org/10.1029/2020GL091216

Tilling, R. L., Ridout, A., Shepherd, A., & Wingham, D. J. (2015). Increased arctic sea ice volume after anomalously low melting in 2013. *Nature Geoscience*, *8*(8), 643–646. https://doi.org/10.1038/NGEO2489

Trevisani, S., Teza, G., & Guth, P. L. (2023). Hacking the topographic ruggedness index. *Geomorphology*, *439*, 108838. https://doi.org/https://doi.org/10.1016/j.geomorph.2023.108838

Villadsen, H., Deng, X., Andersen, O. B., Stenseng, L., Nielsen, K., & Knudsen, P. (2016). Improved inland water levels from SAR altimetry using novel empirical and physical retrackers. *Journal of Hydrology*, *537*, 234–247. https://doi.org/10.1016/j.jhydrol.2016.03.051

Wilson, M. F. J., O'Connell, B., Brown, C., Guinan, J. C., & Grehan, A. J. (2007). Multiscale terrain analysis of multibeam bathymetry data for habitat mapping on the continental slope. *Marine Geodesy*, *1-2*, 3–35. https://doi.org/10.1080/01490410701295962

Wingham, D. J., Francis, C. R., Baker, S., Bouzinac, C., Brockley, D., Cullen, R., de Chateau-Thierry, P., Laxon, S. W., Mallow, U., Mavrocordatos, C., Phalippou, L., Ratier, G., Rey, L., Rostan, F., Viau, P., & Wallis, D. W. (2006). CryoSat: A mission to determine the fluctuations in earth's land and marine ice fields. *Advances in Space Research*, *37*(4), 841–871. https://doi.org/https://doi.org/10.1016/j.asr.2005.07.027

Wingham, D. J., Ridout, A. J., Scharroo, R., Arthern, R. J., & Shum, C. K. (1998). Antarctic elevation change from 1992 to 1996. *Science*, *282*(5388), 456–458. https://doi.org/10.1126/science.282.5388.456

Wingham, D. J., Siegert, M. J., Shepherd, A., & Muir, A. S. (2006). Rapid discharge connects antarctic subglacial lakes. *Nature*, *440*(7087), 1033–1036.

Wingham, D., Rapley, C., & D, G. (1986, September). New techniques in satellite altimeter tracking systems. *IGARSS 86 Symposium*.

Zevenbergen, L. W., & Thorne, C. R. (1987). Quantitative analysis of land surface topography. *Earth Surface Processes and Landforms*, *12*(1), 47–56. https://doi.org/10.1002/esp.3290120107

Zinck, A.-S. P., Wouters, B., Lambert, E., & Lhermitte, S. (2023). Unveiling spatial variability within the dotson melt channel through high-resolution basal melt rates from the reference elevation model of antarctica. *The Cryosphere*, *17*(9), 3785–3801. https://doi.org/10.5194/tc-17-3785-2023